

Unlocking photodetection for quantum sensing with Bayesian likelihood-free methods and deep learning

Mateusz Molenda,^{1,*} Lewis A. Clark ,^{2,3} Marcin Płodzień ,⁴ and Jan Kołodzyński ^{1,†}

¹*Institute of Physics, Polish Academy of Sciences, Aleja Lotników 32/46, 02-668 Warsaw, Poland.*

²*Quantum Innovation Centre (Q.InC), Agency for Science Technology and Research (A*STAR),*

2 Fusionopolis Way, Innovis #08-03, Singapore 138634, Republic of Singapore

³*Institute of High Performance Computing (IHPC), Agency for Science,*

*Technology and Research (A*STAR), 1 Fusionopolis Way,*

#16-16 Connexis, Singapore 138632, Republic of Singapore

⁴*Qilimanjaro Quantum Tech, Carrer de Venezuela 74, 08019 Barcelona, Spain*

(Dated: February 24, 2026)

To operate quantum sensors at their quantum limit in real time, it is crucial to identify efficient data inference tools for rapid parameter estimation. In photodetection, the key challenge is the fast interpretation of click-patterns that exhibit non-classical statistics—the very features responsible for the quantum enhancement of precision. We achieve this goal by comparing Bayesian likelihood-free methods with ones based on deep learning (DL). While the former are more conceptually intuitive, the latter, once trained, provide significantly faster estimates with comparable precision and yield similar predictions of the associated errors, challenging a common misconception that DL lacks such capabilities. We first verify both approaches for an analytically tractable, yet multiparameter, scenario of a two-level system emitting uncorrelated photons. Our main result, however, is the application to a driven nonlinear optomechanical device emitting non-classical light with complex multiclick correlations; in this case, our methods are essential for fast inference and, hence, unlock the possibility of distinguishing different photon statistics in real time. Our results pave the way for dynamical control of quantum sensors that leverage non-classical effects in photodetection.

I. INTRODUCTION

The observation that non-classical resources, specifically, entanglement and squeezing [1–5], allow for measurement precision significantly surpassing the classical limit has ignited a wave of breakthroughs in quantum sensing. Over the past two decades, quantum-enhanced metrology has enabled significant advances across a variety of platforms, including optical clocks [6–9], magnetometers [10–13], interferometers [14–16], and gravitational-wave detectors [17, 18].

The quantum sensors demonstrated in these works predominantly employ interferometric or homodyne detection architectures [19–22], where the physical signal is linearly encoded as a phase shift and extracted by interference with a strong local oscillator or reference field [23, 24]. This often allows the system degrees of freedom, as well as the measurement outcomes, to be described by employing the Gaussian formalism [25, 26]. Crucially, this enables the integration of fast signal-processing solutions in real time for both estimation, e.g., Kalman or Wiener filters [19, 20], and feedback, e.g., linear-quadratic-Gaussian (LQG) control [21, 22].

In contrast, *time-resolved photodetection* [27]—ubiquitous in time-correlated single-photon counting (TCSPC) [28] and widely employed across quantum platforms [29–34]—remains uncommon in sensing ap-

plications. This is because real-time parameter estimation from photoclick patterns poses a major challenge [35]. The complexity of the quantum dynamical description—including environmental noise, detection imperfections, and the stochastic nature of the measurement process [36]—renders direct likelihood evaluation computationally prohibitive [37]. Except for systems of very small dimension [38–41], standard Bayesian inference becomes then intractable in real time [42]. In particular, established techniques such as particle filters (sequential) or Markov-Chain Monte Carlo (batch) [43–45], which rely on frequent likelihood evaluations, fail to bypass the underlying computational bottleneck.

In this work, we show that this bottleneck can be overcome via two distinct approaches: (i) avoiding likelihood computation by resorting to likelihood-free Bayesian inference, specifically *Approximate Bayesian Computation* (ABC) [46–48]; and (ii) employing pre-trained *deep learning* (DL) models [49]. While ABC was only recently proposed for quantum inference [37]—following earlier applications in Hamiltonian learning [50–52]—DL has emerged as a powerful framework in quantum metrology for developing estimation [53–55] and control [56–58] strategies. These include techniques for maximising the Quantum Fisher Information [59, 60] and implementing adaptive Bayesian parameter estimation [61] in photonic interferometry [62–64]. Here, we demonstrate that both ABC and DL methods can extract informative representations from fixed-length photoclick trajectories. In particular, they exploit quantum correlations embedded in such patterns, thereby enabling real-time quantum enhancement in photodetection-based quantum sensors.

* mmolenda@ifpan.edu.pl

† jankolo@ifpan.edu.pl

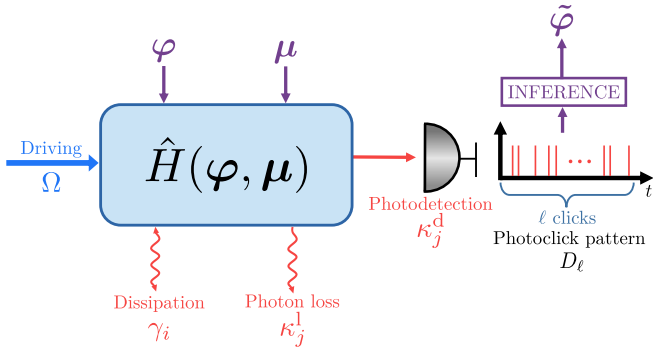


FIG. 1. **Quantum sensing scheme with photodetection.** A quantum system is governed by a Hamiltonian $\hat{H}(\varphi, \mu)$, where φ and μ are vectors of estimated and control parameters, respectively. The system is driven by an external (classical, blue) field (e.g., strong light-beam) of strength Ω and dissipates through multiple (quantum, red) channels with rates γ_i . Photon emission constitutes a separate dissipation process, being further divided into detected and lost channels with rates κ_j^d and κ_j^l , respectively. Upon registering ℓ photons, the most accurate estimator of parameters $\hat{\varphi}$ should be constructed based on the recorded photoclick pattern D_ℓ —a vector of waiting times between consecutive clicks.

The manuscript is organised as follows. In Sec. II, we describe a general quantum sensing scheme that involves a driven quantum system being measured via photodetection. In Sec. III, we detail the inference methods employed (ABC in Sec. III B and DL in Sec. III C); we verify these techniques using a two-level atomic model before focusing on a nonlinear optomechanical system. Section IV presents the main results of our work, and we offer concluding remarks and an outlook in Sec. V.

II. QUANTUM SENSING WITH PHOTODETECTION

The relevant sensing scenario is depicted in Fig. 1, in which a quantum sensor is monitored by probing the light it emits; in particular, the arrival times of photons being continuously detected. By $\varphi = \{\varphi_1, \varphi_2, \dots, \varphi_d\}$ we denote the vector containing the *estimated parameters*, whose values shall be inferred from a particular *photoclick pattern*, i.e., a vector $D_\ell := \{\Delta t_1, \Delta t_2, \dots, \Delta t_\ell\}$ which contains time intervals (waiting times) between consecutive ℓ photoclicks. However, within the framework we allow other *control parameters* μ , whose value is known but should be adjusted for best estimation performance. Moreover, the sensor is considered to be classically driven by some external field of strength Ω . As a result, although the sensing process is modelled dynamically, the instantaneous and steady-state behaviour of the sensor, given a particular form of its dissipation (γ -channels) and detection (κ -channels), can be modified by varying Ω .

The goal is to estimate most accurately parameters φ based on the detected photoclick data D_ℓ . In the idealis-

tic scenario, this should be performed in real time as the successive clicks are recorded. On one hand, this opens door for sensing parameters φ that change in time, with their time-variation being then tracked “on the fly”. On the other, this allows for adjusting the control parameters μ in between clicks, so that the sensing performance is optimised. All this, however, takes for granted that the inference part can be done sufficiently fast. Here, we make the first important step by proposing necessary estimation methods and test their accuracy when sensing *constant parameters* φ for a photoclick trajectories of *fixed length* D_ℓ . Our work lays the groundwork for developing real-time estimation protocols that can be implemented in future photodetection experiments, eventually allowing for the integration of feedback and control.

A. Quantum system with driving and dissipation

Considering a general Hamiltonian describing the system used as a sensor, see Fig. 1, which depends on the estimated φ and control μ parameters, we may decompose it into its free and driving parts, i.e.:

$$\hat{H} \equiv \hat{H}(\varphi, \mu) = \hat{H}_{\text{free}} + \hat{H}_{\text{drive}}(\Omega) \quad (1)$$

with the latter depending explicitly on the driving strength Ω . Although the form of each is unspecified (and may arbitrarily depend on φ and μ), we are motivated by scenarios in which \hat{H}_{free} carries nonlinear interactions that allow to engineer the statistics of emitted photons [65, 66], i.e., control their quantum bunching or anti-bunching properties [67, 68].

Furthermore, to incorporate dissipation of the quantum sensor, we consider its evolution to be described by the Gorini-Kossakowski-Sudarshan-Lindblad (GKSL) master equation [69]:

$$\frac{d\hat{\rho}}{dt} = -\frac{i}{\hbar}[\hat{H}, \hat{\rho}] + \sum_i \gamma_i \left(\hat{L}_i \hat{\rho} \hat{L}_i^\dagger - \frac{1}{2} \{ \hat{L}_i^\dagger \hat{L}_i, \hat{\rho} \} \right) \quad (2)$$

where γ_i are the dissipation rates, and \hat{L}_i are the corresponding Lindblad operators. As a result, we obtain a broad description of sensor dynamics, incorporating both the unitary evolution, which contains the estimated and control parameters, and arbitrary irreversible processes that take a semigroup (Markovian) form (2) [69].

B. Photodetection measurement and unravellings

In order to incorporate the photodetection measurement into the dynamical description, we resort to the continuous measurement theory [24, 36] and, as depicted also in Fig. 1, account for distinct detection channels (light modes) labelled by j , via which the information is extracted from the quantum sensor. In particular, each

of their outputs is measured at a rate $\bar{\kappa}_j^d$ with a photodetector, whose finite efficiency in turn increases κ_j^1 —the effective rate of photon loss in each channel.

Assuming that the continuous measurement does not alter the form of Eq. (2) [70], we arrive at a stochastic master equation that describes the *true evolution* of the system in Fig. 1 when conditioned on a particular photoclick record (trajectory) [71]:

$$d\hat{\rho} = -\frac{i}{\hbar}[\hat{H}, \hat{\rho}] + \sum_i \gamma_i \left(\hat{L}_i \hat{\rho} \hat{L}_i^\dagger - \frac{1}{2} \{ \hat{L}_i^\dagger \hat{L}_i, \hat{\rho} \} \right) dt \quad (3a)$$

$$+ \sum_j \kappa_j^1 \left(\hat{c}_j \hat{\rho} \hat{c}_j^\dagger - \frac{1}{2} \{ \hat{c}_j^\dagger \hat{c}_j, \hat{\rho} \} \right) dt + \mathcal{J}_{\kappa_j^d}[\hat{\rho}], \quad (3b)$$

where \hat{c}_j is the photonic annihilation operator in the j th detection channel, and each photodetection superoperator $\mathcal{J}_{\kappa_j^d}$ is defined as:

$$\mathcal{J}_{\kappa_j^d}[\hat{\rho}] := \kappa_j^d \text{Tr}(\hat{c}_j^\dagger \hat{c}_j \hat{\rho}) \hat{\rho} dt + \left(\frac{\hat{c}_j \hat{\rho} \hat{c}_j^\dagger}{\text{Tr}(\hat{c}_j^\dagger \hat{c}_j \hat{\rho})} - \hat{\rho} \right) dN_t^{\kappa_j^d}, \quad (4)$$

where $dN_t^{\kappa_j^d}$ denotes a Poisson increment taking values 0 or 1 [72], depending whether a photon was detected or not within a time increment dt . The mean of a Poisson increment, or equivalently $P(dN_t^{\kappa_j^d} = 1)$, is given by $\langle dN_t^{\kappa_j^d} \rangle = \kappa_j^d \text{Tr}(\hat{c}_j^\dagger \hat{c}_j \hat{\rho}) dt$ for a given time t .

In particular, the photoclick pattern D_ℓ shown in Fig. 1 describes a particular detection trajectory for the channel j , along which the system evolves according to Eq. (3) with $dN_t^{\kappa_j^d}$ taking value zero at all times apart from the moments at which each of the ℓ clicks is registered. Although we allow multiple detection channels for generality—each photoclick within a pattern D_ℓ also carries information about its type (label j)—note that in the extreme case when all the photons are lost within some channel j , i.e., $\kappa_j^d = 0$, $\kappa_j^1 > 0$, then, as it introduces solely dissipation, it can be equivalently included as another $\gamma_i = \kappa_j^1$ with $\hat{L}_i = \hat{c}_j$ in Eq. (3a).

We also consider the *full unravelling* of the master equation (2), which governs the conditional evolution of the system state under the unphysical assumption that all the processes yielding quantum jumps are monitored [73–75]:

$$d\hat{\rho} = -\frac{i}{\hbar} \left(\hat{H}_{\text{cond}} \hat{\rho} - \hat{\rho} \hat{H}_{\text{cond}}^\dagger \right) dt + \sum_i \mathcal{J}_{\gamma_i}[\hat{\rho}] + \sum_j \mathcal{J}_{\kappa_j^1}[\hat{\rho}] + \mathcal{J}_{\kappa_j^d}[\hat{\rho}], \quad (5)$$

where the conditional (non-Hermitian) Hamiltonian is defined as

$$\hat{H}_{\text{cond}} := \hat{H} - \frac{i\hbar}{2} \sum_i \gamma_i \hat{L}_i^\dagger \hat{L}_i - \frac{i\hbar}{2} \sum_j \kappa_j \hat{c}_j^\dagger \hat{c}_j \quad (6)$$

with $\kappa_j := \kappa_j^1 + \kappa_j^d$ for each j . In particular, when evolving $\hat{\rho}$ only according to the first term in Eq. (5), the special conditional trajectory is recovered that corresponds to *no jumps* occurring and, hence, none of them being registered. Although such system dynamics is trace non-preserving, the state norm at time t directly provides the probability of no-jump occurring until the given t .

Importantly, in Eq. (5) not only jumps associated with unobserved photons are accounted for, but also ones arising due to each dissipative processes labelled by i , i.e.:

$$\mathcal{J}_{\gamma_i}[\hat{\rho}] := \gamma_i \text{Tr}(\hat{L}_i^\dagger \hat{L}_i \hat{\rho}) \hat{\rho} dt + \left(\frac{\hat{L}_i \hat{\rho} \hat{L}_i^\dagger}{\text{Tr}(\hat{L}_i^\dagger \hat{L}_i \hat{\rho})} - \hat{\rho} \right) dN_t^{\gamma_i} \quad (7)$$

with the stochastic Poisson increment now satisfying $\langle dN_t^{\gamma_i} \rangle = \gamma_i \text{Tr}(\hat{L}_i^\dagger \hat{L}_i \hat{\rho}) dt$, which may not possess physical interpretation despite reproducing the correct dissipative dynamics when averaged over.

Although the conditional evolution of the system that is based only on physical observations has to be computed using Eq. (3), Eq. (5) proves to be useful, as it describes a pure-state evolution along each trajectory. Hence, it is much less demanding computationally, as it involves only the wavefunction description instead of the density matrix [73–75]. In particular, if one is interested in generating examples of photoclick patterns, D_ℓ , and not the actual evolution of the system, one may generate these with help of Eq. (5) by *disregarding* the inaccessible (unphysical) clicks (events) in a record—these arise when any of $dN_t^{\gamma_i}$ or $dN_t^{\kappa_j^d}$ takes the value 1.

This does not conflict the fact that *averaging* over inaccessible events—specifically, all the state trajectories generated with Eq. (5) that yield the same record of accessible detection events—consistently recovers the conditional state dynamics (3). Furthermore, by averaging over all potential trajectories without fixing the pattern of detection events ($dN_t^{\kappa_j^d}$), the reduced dynamics described by the original master equation (2) is reproduced.

C. Photoclick pattern as a temporal point process

The record of a photodetection process constitutes a realisation of a stochastic *temporal point process* (TPP), where the recorded data D_ℓ consists of a sequence of photon waiting times $\{X_i\}_{i=1}^\ell$ —see Fig. 2(a). Broadly speaking, TPPs are categorised as either *renewal* or *history-dependent* [76]. In a renewal process, the probability of an event depends solely on the time elapsed since the most recent event. Such processes are characterised by independent and identically distributed (i.i.d.) waiting times, with their statistics thus being fully captured by a single *waiting-time distribution* $w(\tau)$, e.g., the one sketched in Fig. 2(a). In contrast, a history-dependent TPP cannot be described by a single distribution, as the statistics of subsequent events are conditioned on the history of prior detections in a non-trivial manner.

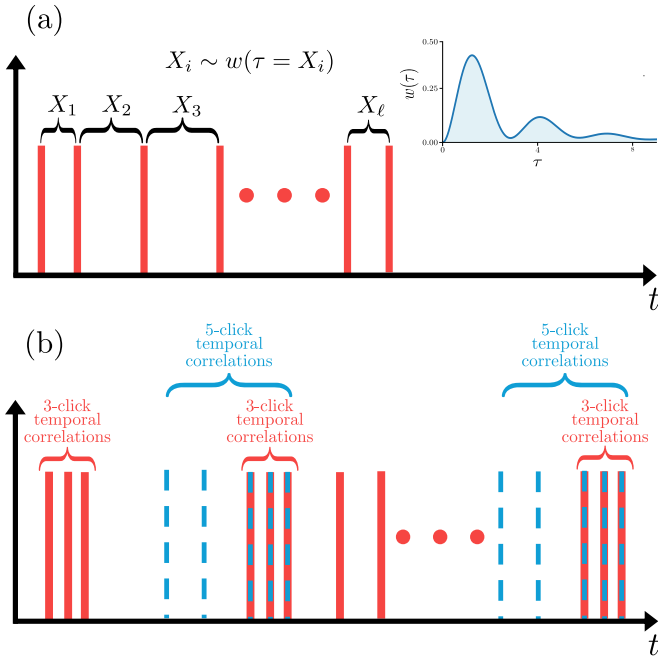


FIG. 2. **Interpreting photodetection as a temporal point process (TPP).** (a) *Renewal TPP*: Waiting times $X = \{X_1, X_2, \dots, X_\ell\}$ are independently and identically distributed (i.i.d.), sampled from a stationary waiting-time distribution $w(\tau)$; (b) *History-dependent TPP*: Waiting times are not i.i.d. and cannot be described by a single distribution. As illustrated, specific records may exhibit hierarchical temporal correlations—such as three-click patterns nested within larger five-click sequences. Any such multi-time correlations require a non-renewal framework to account for quantum effects like photon (anti)bunching [67], which are essential for quantum-enhanced sensing tasks.

In the quantum setting, a *two-level system* (TLS) serves as the paradigmatic renewal source; because the system resets to its ground state upon emission, the memory of prior events is effectively erased [35, 77]. Conversely, most quantum systems possess complex energy-level structures that generate short- or long-lived memory dependencies. These are manifested as temporal correlations in the photoclick pattern that cannot be described by a single distribution [78], as illustrated in Fig. 2(b). Crucially, it is these multi-time correlations that facilitate quantum-enhanced sensing, as they possess significant additional information about estimated parameters beyond what is available in lower-order statistics [79–82].

As shown in Fig. 2(b), non-renewal photoclick patterns can exhibit hierarchical correlations—where fast three-click clusters are nested within broader five-click sequences emergent at larger timescales. Formally, this corresponds to the regime where higher-order correlation functions, specifically third-order $g^{(3)}(\tau_1, \tau_2)$ or higher [83], exhibit non-classical signatures. This is in stark contrast to the renewal framework, where the i.i.d. nature of the waiting times ensures that the second-order $g^{(2)}(\tau)$ -function, being the Laplace transform of

$w(\tau)$, completely determines all higher-order correlations; in such cases, $g^{(n)}$ provides no information beyond what is already captured by the second-order statistics [84, 85]. Consequently, while renewal processes may exhibit non-classical features like antibunching [67], they are fundamentally limited for quantum-enhanced estimation as they cannot exploit the higher-order dependencies that typically drive significant sensitivity gains.

However, extracting this higher-order information poses a formidable challenge; the likelihood functions for history-dependent processes are computationally intensive to evaluate, making parameter estimation significantly more difficult than for renewal processes [37, 39]. This overhead currently precludes the use of non-renewal TPPs in real-time applications, such as active feedback or closed-loop quantum control, where estimation must occur on timescales faster than the system dynamics.

III. EFFICIENT INFERENCE FROM PHOTOCCLICK PATTERNS

Under the Bayesian paradigm, the d parameters to be estimated, $\varphi \in \mathbb{R}^d$, are treated as random variables rather than fixed constants. Their prior distribution, $p(\varphi)$, represents then the *a priori* knowledge about their potential values before any measurements are taken. Given a set of measurement data D , the optimal parameter estimator, $\tilde{\varphi}(D)$, is typically constructed by minimising the average *Mean Squared Error* (MSE) [86]:

$$\text{MSE}[\tilde{\varphi}] := \int d\varphi p(\varphi) \int dD p(D|\varphi) \|\tilde{\varphi}(D) - \varphi\|^2, \quad (8)$$

where $p(D|\varphi)$ is the likelihood distribution—describing probability of obtaining data D given specific parameter values φ —and $\|\cdot\|$ denotes the Euclidean norm between the true parameter vector φ and its estimate $\tilde{\varphi}(D)$.

The optimal estimator that minimises the MSE (8) is generally the mean of the posterior distribution [86]:

$$\hat{\varphi}_{\text{optim}} := \mathbb{E}_{p(\varphi|D)}[\varphi] = \int d\varphi \varphi p(\varphi|D), \quad (9)$$

where the posterior distribution, representing the updated belief about the parameters φ after observing the data D (*a posteriori*), is given by the Bayes' rule [86]:

$$p(\varphi|D) = \frac{p(D|\varphi)p(\varphi)}{p(D)} = \frac{p(D|\varphi)p(\varphi)}{\int d\varphi p(D|\varphi)p(\varphi)}. \quad (10)$$

However, computing Eq. (10) is typically intractable, even numerically. While exhaustive integration or sampling over the φ -parameter space can often be avoided using methods like particle filters (sequential) or Markov-Chain Monte Carlo (batch) [43–45], these techniques remain insufficient if computing the likelihood $p(D|\varphi)$ itself is infeasible. This is particularly relevant for quantum systems with states spanning high-dimensional Hilbert

spaces [37]. In real-time scenarios, such as the photodetection scheme of Fig. 1, calculating the likelihood requires the system state to be continuously updated in response to real-time measurement data—accounting for every individual click in the photoclick pattern in Fig. 1.

Given the complexity of non-renewal quantum systems, recall Fig. 2(b), the challenge is not merely to optimise likelihood evaluation, but to bypass it entirely during the inference stage. In what follows, we explore likelihood-free inference methodologies that shift the computational burden away from real-time execution. First, we describe a Bayesian approach to estimation based on ABC, which circumvents the likelihood bottleneck by comparing observed data with simulated samples [37]. We then present an alternative approach using DL, where the same simulated data is used to train *Deep Neural Networks* (DNNs) offline. While ABC naturally provides estimation errors and a reconstructed posterior, we demonstrate that DNNs can be similarly configured to provide these metrics. This allows us to use both methods as a mutual benchmark for performance in real-time quantum parameter estimation.

A. Data preprocessing and sufficient statistics

Effective *data preprocessing* can significantly improve the accuracy and computational efficiency of estimation tasks. Here, we treat preprocessing as the construction of *summary statistics*—a mapping \mathcal{S} that transforms the raw data into a lower-dimensional representation capturing its key features:

$$\bar{D} := \mathcal{S}(D), \quad (11)$$

where in case of photodetection D represents a general TPP trajectory of a finite length (D_ℓ in Fig. 2) and \bar{D} denotes the preprocessed data. Within this framework, we define *sufficient summary statistics* as a special preprocessing \mathcal{S} that retains all information about the parameters φ contained in the original data; formally, this occurs if the posterior can be expressed as:

$$p(\varphi|\mathcal{S}(D)) = p(\varphi|D). \quad (12)$$

Selecting an adequate sufficient summary statistic is non-trivial and relies heavily on the physical intuition of the problem. For instance, in any renewal TPP of Fig. 2(a), the *histogram of waiting times* serves as a sufficient summary statistic. Because the waiting-time distribution, $w(\tau)$ in Fig. 2(a), uniquely and completely defines a renewal process, its empirical representation—the histogram—captures all the information available for estimation [37].

B. Approximate Bayesian Computation

To overcome the bottleneck of likelihood computation, we turn our attention first to likelihood-free inference,

specifically *Approximate Bayesian Computation* (ABC). This framework bypasses direct evaluation of the likelihood function by leveraging data simulations [46, 47]. The core logic of ABC is straightforward: rather than constructing $p(D|\varphi)$ from the model, we use the model as a generative engine. We draw parameter values φ from the prior distribution $p(\varphi)$ and, for each φ , simulate a synthetic trajectory D' (or draw it from a precomputed library). We then compare the simulated dataset D' with the observed data D using a predefined distance measure. If D' is close enough to D to meet a set tolerance ϵ , we retain the specific parameters φ used to generate it. By aggregating these accepted parameter values, we construct an empirical distribution that faithfully approximates the posterior—provided that the number of simulated trajectories is large enough and the distance criterion is sufficiently stringent [46, 47].

Mathematically, ABC yields an approximation of the posterior distribution in the form:

$$q_\epsilon(\varphi|D) \propto p(\varphi) \int dD' \mathbb{I}[\rho(D, D') \leq \epsilon] p(D'|\varphi), \quad (13)$$

where $\rho(D, D') \geq 0$ is a proper distance function quantifying dissimilarity between datasets, and $\mathbb{I}[\cdot]$ is an indicator function that equals 1 when the condition is met and 0 otherwise. As $\epsilon \rightarrow 0$, the approximation converges to the true posterior, albeit at the cost of diminishing acceptance rate—requiring more and more samples D' to be drawn with less and less of them being accepted.

In practice, it is usually infeasible to compare entire datasets directly, especially when they are high-dimensional or continuous. Instead, we identify summary statistics, $\mathcal{S} = \{\mathcal{S}_i\}_i$ each corresponding to a particular preprocessing in Eq. (11), designed together to be nearly sufficient such that $p(\varphi|\mathcal{S}(D)) \approx p(\varphi|D)$. As a result, Eq. (13) can be rewritten as

$$q_\epsilon(\varphi|D) \propto p(\varphi) \int dD' \mathbb{I}[\delta(\mathcal{S}(D), \mathcal{S}(D')) \leq \epsilon] p(D'|\varphi), \quad (14)$$

where δ is now the measure quantifying overall distance between multiple summary statistics evaluated for the two datasets, D and D' .

As before, for a sufficiently small ϵ , the results remain accurate within a marginal error. By employing summary statistics—which can be precomputed and cached for each dataset D' stored—the computation time of $\delta(\mathcal{S}(D), \mathcal{S}(D'))$ becomes negligible. Furthermore, as relevant summary statistics may be shared across multiple datasets, the acceptance rate is improved, thereby accelerating the sampling process. Balancing the acceptance rate against approximation accuracy is a central challenge in any ABC implementation [37].

Note that acceptance criteria can be applied either to each summary statistic individually or jointly through a common, weighted threshold, as in Eq. (14). In this work, however, we set the thresholds individually for convenience whenever multiple summary statistics are used.

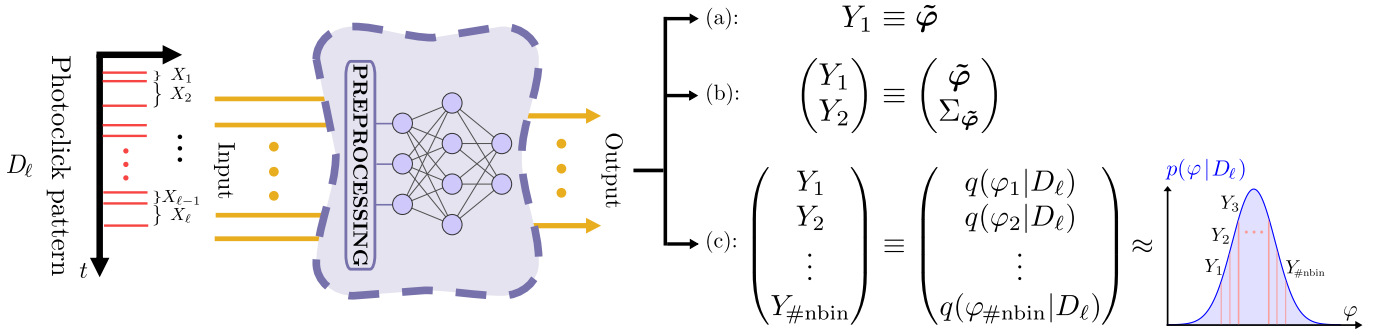


FIG. 3. **Deep learning (DL) inference frameworks considered.** The input of a neural network, $X = \{X_1, X_2, \dots, X_\ell\}$, is set to the sequence of inter-event waiting times for a given photoclick pattern D_ℓ . The output Y is adapted to a specific statistical task: (a) Within the *regression* framework, the network provides point estimates of the parameter vector $\tilde{\varphi}$ by minimising the Mean Squared Error (MSE). (b) In the *probabilistic regression* framework, the network is assumed to yield a Gaussian posterior; thus, the Negative Log-Likelihood (NLL) is employed as the loss function, with the output providing both the parameter estimates and the corresponding errors covariance matrix, $\Sigma_{\tilde{\varphi}}$. (c) In the *classification* framework, which uses Cross-Entropy (CE) as the loss function, the output directly provides a discrete grid-representation of the posterior distribution.

In particular, we replace the joint indicator in Eq. (14) with a product of individual ones, $\mathbb{I}[\delta(\mathcal{S}(D), \mathcal{S}(D')) \leq \epsilon] \rightarrow \prod_i \mathbb{I}[\delta(\mathcal{S}_i(D), \mathcal{S}_i(D')) \leq \epsilon_i]$, allowing us to calibrate each ϵ_i separately [37].

C. Deep learning inference frameworks

In recent years, the rapid evolution of *Deep Learning* (DL) algorithms has enabled their successful deployment across a wide spectrum of problems in quantum physics [87], ranging from quantum state reconstruction [88] to phase classification and anomaly detection [89, 90], as well as in real-time estimation tasks [53, 91–93]. Here, we investigate the performance of three specific DL inference frameworks based on both *regression* and *classification* architectures [49]. While regression is utilised for direct point-parameter estimation and uncertainty quantification, the classification framework allows for a non-parametric reconstruction of the full posterior distribution. A comparative analysis of these schemes allows us to assess the trade-offs between computational efficiency and the fidelity of the inferred statistics in the quantum scenarios considered.

As presented in Fig. 3, here the input to the neural network is always a TPP trajectory D_ℓ . To ensure compatibility with the ABC and enhance learning efficiency, we allow for preprocessing the raw data via a summary statistic, i.e., $\bar{D}_\ell = \mathcal{S}(D_\ell)$. Such a transformation can significantly improve DL performance if \mathcal{S} is chosen to distil the key dynamical features of photoclick patterns D_ℓ . For instance, in scenarios where D_ℓ follow a renewal process, constructing a histogram of waiting times can be highly beneficial [35, 38, 39], as it provides a sufficient statistic for the data representation.

1. MSE-based estimation as a regression problem

Regression, a fundamental task in supervised machine learning, involves learning a mapping from input features to continuous-valued target variables [49]. The general model description is depicted in Fig. 3(a). The model is trained by minimising the MSE between the predicted and true values across a training set $\mathcal{T} = \{D^{(k)}\}_{k=1}^\nu$ of ν independent realisations:

$$\mathcal{L}_{\text{MSE}} := \frac{1}{\nu} \sum_{k=1}^{\nu} \left\| \tilde{\varphi}(D^{(k)}) - \varphi^{(k)} \right\|^2, \quad (15)$$

where $\varphi^{(k)}$ refers to the vector of true parameter values for the k -th sample and $\tilde{\varphi}(D^{(k)})$ are the corresponding model's predictions based on the input photoclick dataset $D^{(k)}$. Here, $\|\cdot\|$ denotes the Euclidean distance between them. The MSE loss penalises larger errors more heavily and is standard in regression tasks due to its smoothness and convexity properties.

Moreover, as demonstrated in Ref. [94], for Stochastic Gradient Descent (SGD)-based Deep Neural Networks (DNNs), the probability of converging to a generalising function f given a training set \mathcal{T} , denoted $P_{\text{SGD}}(f|\mathcal{T})$, closely approximates the Bayesian posterior over functions $P(f|\mathcal{T})$, particularly in the over-parametrised regime. This similarity also holds for variants of SGD, such as Adam, Adagrad, Adadelata, and RMSprop. In cases where the Bayesian posterior is highly biased toward simple functions, SGD-like optimisers tend to sample these simple, better-generalising functions with high probability, behaving—to first order—like Bayesian samplers. This behaviour is consistent across various architectures, including Multi-Layer Perceptrons (MLP), Convolutional Neural Networks (CNN), and Long Short-Term Memory (LSTM) networks [49].

Consequently, the output of a regression DNN, $\tilde{\varphi}(D) = f(D)$, can be interpreted as an estimate derived from a

learned mapping that structurally reflects the Bayesian posterior distribution over the function space. Hence, given that the MSE (8) is used as the training objective (15), the network converges to a point estimator that, as discussed around Eqs. (8-10), effectively approximates the posterior mean.

2. Probabilistic regression under Gaussian approximation

While standard regression models provide point estimates, typically corresponding to the posterior mean, they do not capture the structure of the posterior distribution. As a result, these models cannot quantify uncertainty or provide error estimates. A natural approach to address this limitation is through *probabilistic regression* methods [95], in which the network is forced to output also other parameters of the posterior distribution, whose form is assumed to belong to a particular class. A common and often effective way is to model the posterior distribution as approximately Gaussian [96, 97].

Under this assumption, the network can be trained to predict both the parameters φ and their covariance Σ_φ , as shown in Fig. 3(b), by using the *Negative Log-Likelihood* (NLL) as loss function, which encourages the model to output not only the best-fit prediction but also an estimate of the associated uncertainty:

$$\mathcal{L}_{\text{NLL}} := \frac{1}{\nu} \sum_{k=1}^{\nu} \left[\left(\tilde{\varphi}(D^{(k)}) - \varphi^{(k)} \right)^T (\Sigma^{(k)})^{-1} \times \right. \\ \left. \times \left(\tilde{\varphi}(D^{(k)}) - \varphi^{(k)} \right) + \frac{1}{2} \ln |\Sigma^{(k)}| \right], \quad (16)$$

where $\tilde{\varphi}(D^{(k)})$ are the predicted parameters for the k -th data point $D^{(k)}$, and $\Sigma^{(k)}$ is their predicted covariance matrix. The true value of the parameter is denoted $\varphi^{(k)}$, and ν is the total number of samples. In order to efficiently compute the loss function, the Cholesky decomposition for the covariance is used, $\Sigma = AA^T$, where A is a lower triangular matrix that can be parametrised by $d(d+1)/2$ values. Thus, strictly speaking, the network outputs the vector of predicted parameter values, $\tilde{\varphi}$, and the predicted entries of A , from which the covariance matrix, $\Sigma_{\tilde{\varphi}}$, is straightforwardly reconstructed.

3. Posterior reconstruction by means of classification

Finally, to enable the DL model to reconstruct the posterior distribution directly without prior assumptions regarding its functional form (e.g., Gaussianity), we employ the supervised *classification* framework [49]. In this setting, the continuous parameter space is discretised into a d -dimensional grid of potential values. During training, each input photoclick pattern $D^{(k)}$ is associated with a discrete class label corresponding to its ground-truth parameters $\varphi^{(k)}$; however, the trained network predicts a

probability distribution across the entire grid, providing a discrete approximation of the full posterior, as illustrated in Fig. 3(c) (shown in one dimension for simplicity).

The model is trained using the *Cross-Entropy* (CE) loss:

$$\mathcal{L}_{\text{CE}} := - \sum_{k=1}^{\nu} \sum_{n=1}^{\#\text{nbins}} \delta_{\varphi^{(k)}, \varphi_n} \log \left[q(\varphi_n | D^{(k)}) \right] \quad (17)$$

where $q(\varphi_n | D^{(k)})$ is the output of the DNN associated with the bin labelled by n evaluated for the input $D^{(k)}$, whereas φ_n are the parameter values corresponding to that bin. In App. A, we show explicitly that minimisation of the CE (17) is equivalent to minimising the Kullback-Leibler (KL) divergence between the true posterior $p(\varphi | D)$ and the DL-based estimate $q(\varphi | D)$.

Consequently, the resulting network output is a discrete probability mass function over the parameter grid, which directly approximates the posterior distribution. Importantly, this scheme bypasses the intractable evidence integral in Eq. (10), as the posterior is learned directly from a synthetic dataset sampled from the joint distribution $p(D, \varphi)$ (recall Sec. II B).

4. Neural network architectures used

We evaluated several neural network architectures to identify the optimal configuration for each estimation task; further technical details are provided in App. B. For *regression* applied to renewal TPPs, we implement an architecture similar to that in Ref. [38] with preprocessing, where the initial layer computes an empirical histogram of the input waiting times. For history-dependent TPPs, we employ a network composed of LSTM layers [98], followed by a fully connected network. The LSTM cells are a form of recurrent neural network (RNN) architecture specifically designed to process sequential data [49]. By maintaining an internal memory that enables the model to learn complex temporal dependencies, they are well-suited for analysing history-dependent TPP trajectories.

For point estimation using the MSE loss, the output layer provides a single prediction for each parameter. In the case of *probabilistic regression* (NLL loss), the output layer includes additional neurons to parametrise the covariance matrix. Finally, for the *classification* framework, we use one-dimensional convolutional layers (CNN) with max-pooling, followed by a fully connected network. The output layer represents a probability mass function over the discretised parameter grid, from which we derive point estimates by calculating either the mode or the mean of the resulting posterior distribution.

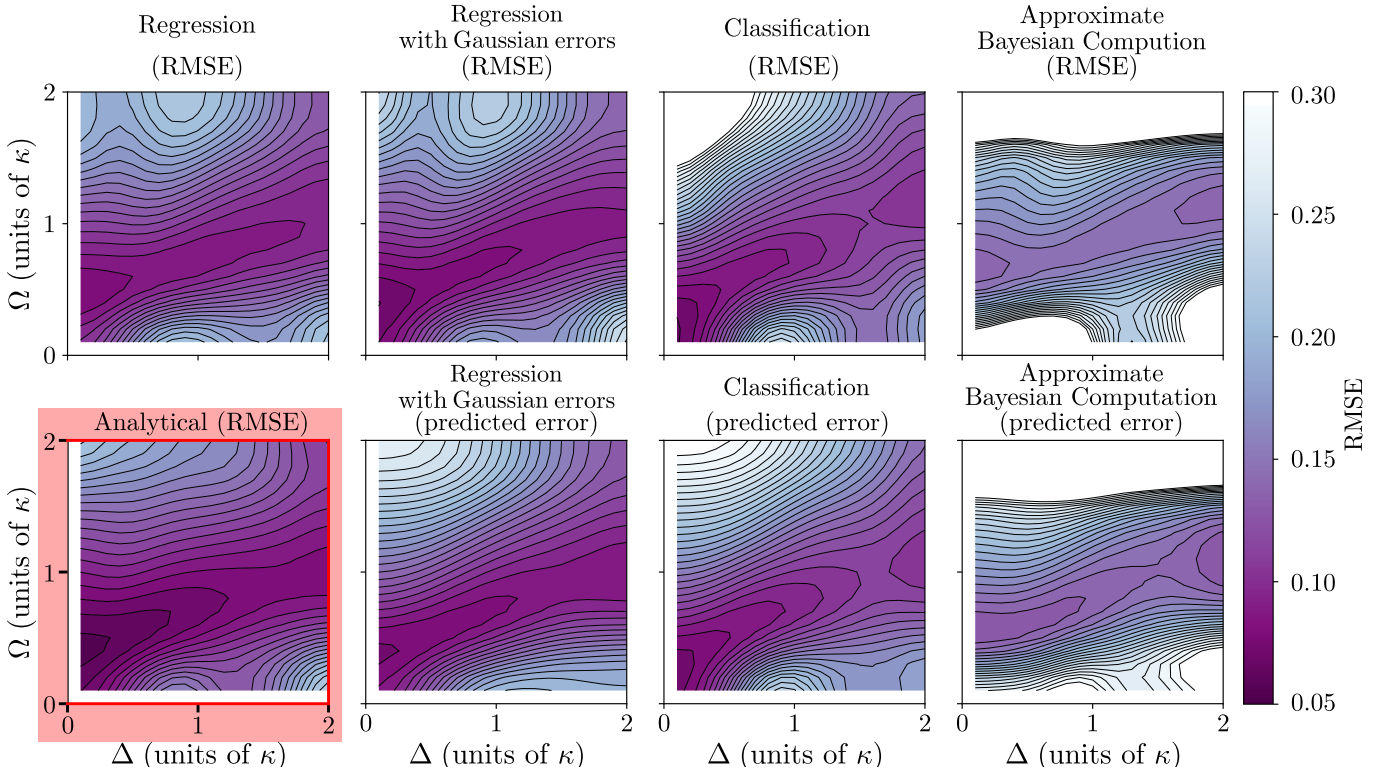


FIG. 4. **Simultaneous estimation of the driving frequency Ω and the laser detuning Δ for a two-level atom.** We compare overall RMSEs, $\sqrt{\text{MSE}[\tilde{\Omega}] + \text{MSE}[\tilde{\Delta}]}$, achieved by the DL and ABC methods considered with the true RMSE (*red frame*) computed analytically, as well as the errors predicted by the methods. In each case a 2D plot of error (RMSE) is shown as a function of estimated parameter values $\Delta, \Omega \in [0, 2]$ (in units of κ). *Top row (from left to right)*: RMSEs attained by the histogram-based regression network, Negative Log-Likelihood (NLL) histogram-based network, CNN classification network and by the ABC method. *Bottom row*: The true RMSE (in red) evaluated based on the waiting-time distribution followed by (*from left to right*) the error predicted by the NLL histogram-based network, CNN classification network and by the ABC method.

D. Verification: Multiparameter sensing with a two-level atom

To verify the ABC and DL approaches to estimation, we first test them in the simple setting of a laser-driven two-level atom, described by the Hamiltonian [99]:

$$H^{\text{atom}} = -\hbar\Delta\hat{\sigma}^+\hat{\sigma}^- + \frac{\hbar\Omega}{2}(\hat{\sigma}^- + \hat{\sigma}^+), \quad (18)$$

where $\hat{\sigma}^+(\hat{\sigma}^-)$ is the atomic raising (lowering) operator. Our goal is to estimate both the laser detuning Δ and the driving frequency Ω .

For the purpose of verification, we assume a single light detection channel of unit efficiency, as described in Sec. II B, with the j -index being redundant and $\kappa^1 = 0$. Crucially, as the atom resets to the ground state after every emission event, photoclick trajectories form a renewal TPP; hence, their statistics are fully characterised by the waiting-time distribution [77]. Consequently, in this special case, both the likelihood and the posterior distribution can be determined analytically [35, 37], providing an ideal benchmark to verify the accuracy of our likelihood-free methods.

in Fig. 4, we present the two-parameter estimation performance for the methods introduced. Since we are dealing with a renewal process, we can simplify the inference problem by incorporating data preprocessing that converts a photoclick trajectory into a histogram without losing information. We compute the relevant RMSEs attained (top row of Fig. 4), which should be compared with the analytical solution (bottom-left of Fig. 4). Moreover, we present the error predictions for the relevant methods (bottom row of Fig. 4).

When implementing ABC (fourth column in Fig. 4), we include the total time as an additional summary statistic alongside the histogram to improve the efficiency of the acceptance criteria [37]. In the case of classification (third column in Fig. 4) and its CNN implementation, we do not preprocess the data, as the network relies on convolution filters applied directly to the photoclick pattern.

All tested methods show good agreement with the analytical results, for both the estimation of parameters and the prediction of errors, which underlines the multiparameter estimation capabilities of the likelihood-free ABC and DL approaches.

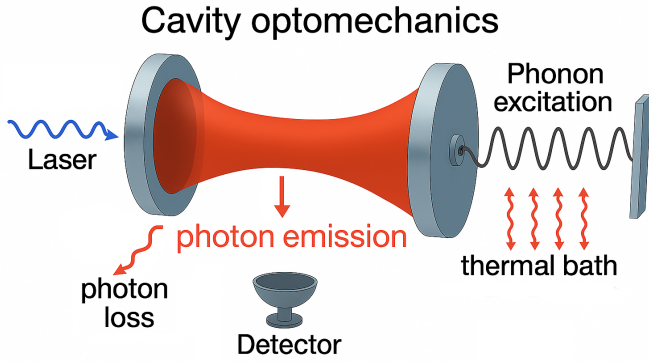


FIG. 5. **Schematic of a generic optomechanical sensor.** An external laser drive populates the optical cavity mode, which couples to a mechanical resonator (e.g., a vibrating mirror, a levitated nanoparticle, or a photonic crystal mode) via radiation pressure. This interaction imprints the mechanical dynamics onto the cavity field, which is then probed by monitoring the photons leaking out via photodetection. The resulting photoclick patterns provide the data for our likelihood-free inference methods.

IV. RESULTS: NONLINEAR OPTOMECHANICAL SENSOR

We now focus on the main application motivating our work, depicted schematically in Fig. 5: a laser-driven optomechanical device [66] whose output light is measured by photodetection. Crucially, when operated in the non-linear regime—when the coupling between its optical (cavity) and mechanical (phonons) degrees of freedom is significant—the system yields non-classical multiclick correlations that can be leveraged for sensing. Moreover, these correlations can be directly controlled by varying the detuning Δ of the laser driving the cavity [82, 100].

This allows us to study the capabilities of both ABC and DL inference frameworks in capturing correlations in photoclick patterns that must be described by history-dependent TPPs, as introduced in Sec. II C. However, in contrast to the case of the two-level atom which yields a renewal TPP, an analytic form for the likelihood or the posterior distribution—and, by extension, the minimal MSE (8) or the optimal estimator (9)—is here intractable. Furthermore, the numerical complexity involved in computing these precludes a direct analysis of optimal estimation performance, as it would require evaluating averages over a vast number of photoclick trajectories. In this regard, the two likelihood-free approaches, ABC and DL, offer the first practical solutions.

Applications of optomechanical devices range from external force and acceleration sensing [101, 102] to broadband displacement and force measurements at and below the standard quantum limit [103, 104]. More recently, schemes involving multiple sensors for distributed force sensing were demonstrated [105] and proposed for dark-matter field searches [106]. These applications are implemented across various platforms, including optically lev-

itated nanoparticles [107, 108] and integrated photonic crystals [109, 110], the latter of which frequently rely on discrete photodetection and photon-correlation statistics [29, 111].

Typically, these scenarios involve estimating parameters (φ in Fig. 1) that enter the mechanical Hamiltonian in a linear fashion, while control parameters (μ in Fig. 1) are properties of the driving laser. However, to evaluate the capacity of ABC and DL for extracting information from multiphoton correlations, we test them in a scenario where the drive detuning, Δ , is the parameter to be estimated. While Δ could be estimated in the absence of mechanics, its variations here directly translate into higher-order correlations emerging via the non-linear interaction with the mechanics—features we intend to capture using ABC and DL inference frameworks.

1. Optomechanical dynamics

The generic optomechanical Hamiltonian relevant for the setup of Fig. 5 is given by [66]:

$$\hat{H} = -\hbar\Delta \hat{a}^\dagger \hat{a} + \hbar\omega_M \hat{b}^\dagger \hat{b} + \frac{\hbar\Omega}{2} (\hat{a} + \hat{a}^\dagger) + \hbar g \hat{a}^\dagger \hat{a} (\hat{b} + \hat{b}^\dagger), \quad (19)$$

where \hat{a} and \hat{b} are the bosonic annihilation operators corresponding to the photonic and phononic modes, respectively. The parameter Δ is the laser detuning, ω_M is the mechanical oscillator frequency, Ω is the laser driving strength, and g characterises the optomechanical coupling.

To capture decoherence effects, we model dissipation through several decay channels. Photons leak out of the optical cavity at a rate κ , while the mechanical oscillator is thermally coupled to a bath, with a damping rate γ , allowing phonons to be spontaneously created or annihilated. The resulting evolution is described by the GKSL master equation [99]:

$$\begin{aligned} \frac{d\hat{\rho}}{dt} = & -\frac{i}{\hbar} [\hat{H}, \hat{\rho}] + \kappa \left(\hat{a} \hat{\rho} \hat{a}^\dagger - \frac{1}{2} \{ \hat{a}^\dagger \hat{a}, \hat{\rho} \} \right) \\ & + \gamma(\bar{m} + 1) \left(\hat{b} \hat{\rho} \hat{b}^\dagger - \frac{1}{2} \{ \hat{b}^\dagger \hat{b}, \hat{\rho} \} \right) \\ & + \gamma\bar{m} \left(\hat{b}^\dagger \hat{\rho} \hat{b} - \frac{1}{2} \{ \hat{b} \hat{b}^\dagger, \hat{\rho} \} \right), \end{aligned} \quad (20)$$

where $\bar{m} = [\exp(\hbar\omega_M/k_B T) - 1]^{-1}$ is the mean phonon occupation number, dictated by the mechanical frequency ω_M and the temperature T of the bath.

2. Simulating photoclick patterns

Following the unravelling procedure described in Sec. II B, we define the conditional Hamiltonian with

Parameter	Symbol	Value	Units
Cavity decay rate	κ	1	(scaled)
Photon detection rate	κ^d	0.9	κ
Mechanical frequency	ω_M	$4\sqrt{2}$	κ
Mechanical damping	γ	$10^{-3}\omega_M$	κ
Optomechanical coupling	g	4	κ
Mean phonon number	\bar{m}	1	—
Laser driving strength	Ω	$0.3\omega_M$	κ
Detuning range	Δ	$[-10, 0]$	κ
Dark count rate (DCR)	λ_{DCR}	10^{-2}	κ

TABLE I. **Optomechanical parameters** assumed in photoclick pattern simulations following Ref. [37].

multiple decay channels:

$$\hat{H}_{\text{cond}} = \hat{H} - \frac{i\hbar}{2}(\kappa\hat{a}^\dagger\hat{a} + \gamma(\bar{m} + 1)\hat{b}^\dagger\hat{b} + \gamma\bar{m}\hat{b}\hat{b}^\dagger). \quad (21)$$

This leads to the full unravelling stochastic master equation (5) of the form:

$$d\hat{\rho} = -\frac{i}{\hbar}[\hat{H}_{\text{cond}}\hat{\rho} - \hat{\rho}\hat{H}_{\text{cond}}^\dagger] dt + \mathcal{J}_{\kappa^d}(\hat{\rho}) + \mathcal{J}_{\kappa^1}(\hat{\rho}) + \mathcal{J}_{\gamma_-}(\hat{\rho}) + \mathcal{J}_{\gamma_+}(\hat{\rho}), \quad (22)$$

where we partition loss into detected (κ^d) and undetected (κ^1) channels ($\kappa^d + \kappa^1 = \kappa$), and obtain also the jump processes, as defined in Eq. (7), responsible for phonon creation (γ_+) and annihilation (γ_-). We generate waiting-time trajectories D_ℓ by simulating click patterns until ℓ photon detections are registered, while ignoring jumps of other types.

In the analysis that follows, we generate photoclick patterns by setting the optomechanical parameters to values consistent with Ref. [37], as summarised in Table I. These values correspond to operation in the sideband-resolved regime [66]. However, we stress that while sideband-resolved dynamics are not strictly required for the inference tasks considered [82], they provide a realistic framework for generating the non-renewal photoclick patterns analysed herein. Furthermore, this regime and the choice of red (negative) detuning, see below, align with the standard physical intuition from linear optomechanics: such a configuration is typically required in sensing applications to avoid heating the mechanical resonator during the measurement process [66].

3. Controlling statistics of emitted photons

In the non-linear regime, radiation pressure induces an energy shift proportional to the square of the cavity photon number, n_{cav} . This shift is reflected in the system's energy spectrum [66, 100]:

$$E(n_{\text{cav}}, n_{\text{mech}}) = -\hbar\Delta n_{\text{cav}} + \hbar\omega_M n_{\text{mech}} - \hbar\frac{g^2}{\omega_M} n_{\text{cav}}^2, \quad (23)$$

where n_{cav} and n_{mech} are the cavity and mechanical occupation numbers, respectively.

By selecting specific detuning regimes, $\Delta_n = -n\frac{g^2}{\omega_M}$ (where $n \in \mathbb{Z}$), one can cancel the non-linear term for a target photon number n . For $n = 1$, single-photon transitions are energetically favoured. For higher integers $n \geq 2$, the cavity resonance is restored specifically for the n -photon manifold, forcing photons to be emitted in correlated groups of size n , resulting in bunched light in the form of pairs ($n = 2$), triplets ($n = 3$), or larger n -photon clusters [66].

These cases are a direct manifestation of photoclick patterns constituting a history-dependent TPP. The delayed mechanical response ensures that once an initial photon is emitted, the cavity remains in a favourable state for $n - 1$ subsequent emissions. This mechanism generates the temporal multiclick correlations that contain the information about system parameters we aim to capture using ABC and DL inference frameworks.

A. Estimation performance

The performance of our inference frameworks—Approximate Bayesian Computation (ABC) and Deep Learning (DL) regression—is compared in Fig. 6. Our primary objective is to minimise the average MSE (8), so we evaluate all models on their ability to approximate the posterior mean. To ensure a consistent and fair comparison, we assume a uniform (flat) prior over the parameter range, matching the distribution used to generate the training data. Crucially, the same dataset of waiting-time trajectories serves both as the training set for the neural networks and as the reference library for the ABC algorithm.

We quantify the precision of our predictions using the Root (Average) Mean Squared Error (RMSE) and by inspecting one-to-one estimation plots in Fig. 6. We observe the emergence of plateaus in one-to-one estimation and aim to reduce them through bias compensation.

1. Approximate Bayesian Computation

We perform estimation over the range $\Delta \in (0, 10)$ by constructing the ABC posterior for each dataset D_ℓ and extracting its mean as the parameter estimator. The ABC algorithm utilises two summary statistics applied to each dataset D'_ℓ (each consisting of $\ell = 80$ photoclicks) drawn from the precomputed library: the average waiting time $\bar{t}_\ell = \frac{1}{\ell} \sum_{i=1}^{\ell} t_i$, and the L^2 -norm between waiting-time histograms:

$$\delta(\mathcal{S}(D_\ell), \mathcal{S}(D'_\ell)) = \sqrt{\sum_i (x_i - x'_i)^2}, \quad (24)$$

where $\mathcal{S}(D_\ell)$ and $\mathcal{S}(D'_\ell)$ are the time-binned histograms of the waiting times for the observed and library-drawn

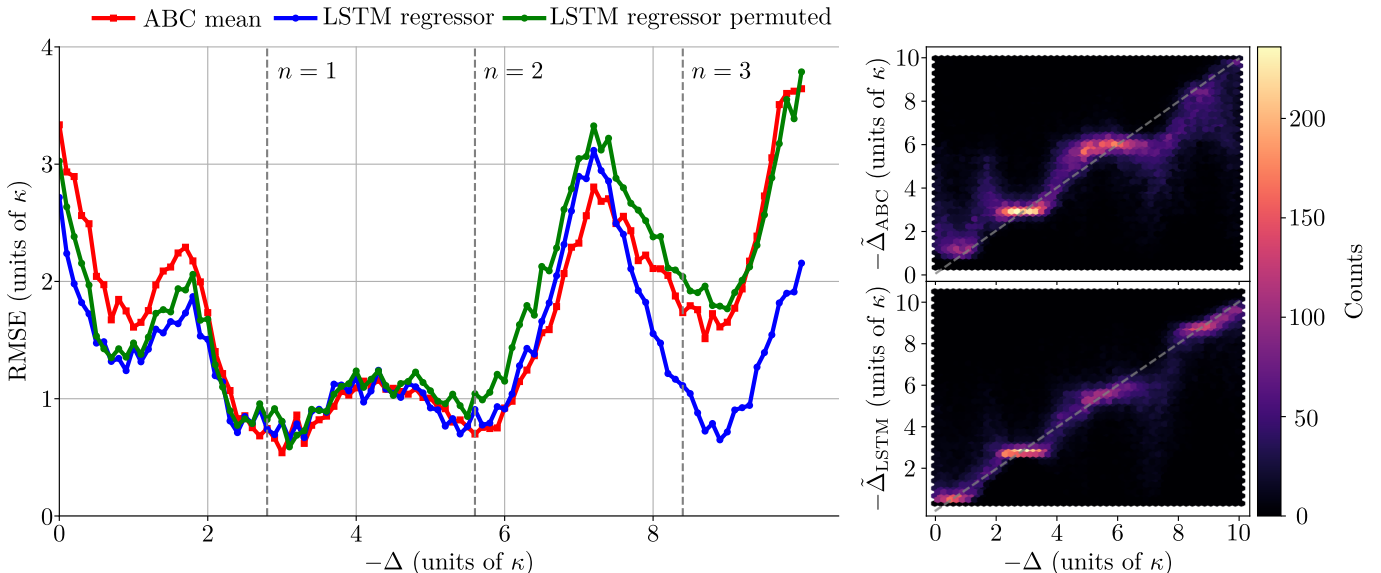


FIG. 6. **Root Mean Squared Error (RMSE) attained with ABC and DL-regression frameworks** as a function of the true detuning Δ . In the *main plot*, the ABC estimator is constructed as the mean of the reconstructed posterior (red), while the regression framework relies on an LSTM architecture trained on raw waiting-time trajectories (blue). The performance of the LSTM regressor when applied to randomly permuted input trajectories is also shown (green). Vertical dashed grey lines indicate the special detuning regimes ($n = 1, 2, 3$) associated with resonance photon statistics. The *right panels* display one-to-one plots of the estimated values $\hat{\Delta}_{ABC}$ (top) and $\hat{\Delta}_{LSTM}$ (bottom) against the true parameter Δ , where colour intensity represents prediction density. The regression framework demonstrates superior accuracy, particularly in the $n = 3$ regime; here, the performance degradation under permutation confirms the model’s ability to exploit history-dependent temporal correlations.

datasets, respectively, with x_i and x'_i denoting the corresponding bin counts.

As seen in Fig. 6 (red), the RMSE attained by ABC exhibits distinct dips near all resonance values. Although the average waiting time statistic is sufficient for the $n = 1$ regime, in the $n = 2$ and $n = 3$ regimes, rapid successive emissions manifest as a shift in the histogram density toward shorter intervals [37]. Notably, the RMSE dip for $n = 3$ is significantly higher than for $n = 1$ or $n = 2$. This limitation suggests that while the chosen summary statistics extract relevant physical information, their reliance on aggregated data fails to capture the information contained within the temporal ordering of photon emissions that becomes critical at $n \geq 3$.

2. Neural Network Regression

To evaluate the DL-based regression approach, we trained and evaluated models based on LSTM, CNN, and Transformer architectures. Here, we present results only for the architecture that achieved the highest performance: the LSTM regressor. Further details regarding the network hyperparameters and training procedures are provided in App. B.

The LSTM regressor (Fig. 6, blue) operates directly on raw trajectories without prior physical knowledge. Its performance matches that of ABC at lower Δ , particularly in the $n = 1$ and $n = 2$ regimes, but it significantly

outperforms ABC at $n = 3$, where it yields an RMSE dip comparable to the other resonances. The equivalence at $n = 1$ is clarified by the Principal Component Analysis (PCA) in App. C, which demonstrates that the total arrival time is the most informative feature for the network to learn in this regime.

To explicitly study the role of the temporal structure learned by the LSTM, we evaluate its performance on *randomly permuted* trajectories (Fig. 6, green). Comparing the blue (raw) and green (permuted) curves reveals the extent to which the network extracts information from higher-order temporal correlations. While the improvement near $n = 2$ is negligible—confirming that the histogram statistic is largely sufficient for pair-bunching—the LSTM achieves significantly lower RMSE in the $n = 3$ regime. Here, random permutations destroy the specific ordering critical to the $n = 3$ manifold, where the LSTM (blue) exploits history-dependent correlations that the ABC summary statistics discard. Conversely, since the LSTM under random permutations (green) is only mildly outperformed by the ABC (red) at $n = 3$, this suggests that the neural network successfully captures the detuning information contained within the histogram statistics even when temporal ordering is lost.

These results are summarised in Table II, which lists the summary statistics used by the ABC algorithm alongside those deduced for the LSTM regressor. It evaluates their respective sufficiency for the $n = 1, 2$, and 3 detuning regimes, providing an explanation for whether the

Detuning Regime	ABC			DL	
	Summary Statistics	Sufficiency	Explanation	Summary Statistics Learnt	Verification
$n = 1$	total time	✓	Effectively a renewal TPP.	total time	PCA analysis, see App. C.
$n = 2$	total time + histogram	✓	Photon-pair emission captured by the histogram.	total time + histogram	Invariance to random permutations, see Fig. 6.
$n = 3$	total time + histogram	✗	A history-dependent TPP with third order correlations.	beyond histogram	Strong sensitivity to trajectory ordering, see Fig. 6.

TABLE II. **Summary statistics crucial to each of the $n = 1, 2, 3$ detuning regimes.** The sufficiency of the summary statistics employed by the ABC algorithm is verified. These are compared with ones learnt by the DL model for each n .

chosen features are adequate to capture the underlying photoclick dynamics.

3. Mitigating Estimation Bias

The right panels of Fig. 6 show the one-to-one comparison between estimated and true parameters. Both frameworks exhibit plateau-like behaviour, though the spread is markedly smaller for the LSTM. The significant degradation of ABC near $n = 3$ highlights the limitation of histogram-based statistics in capturing high-order temporal structures.

These plateaus arise because RMSE minimisation inherently prioritises low estimator variance over low bias. While this bias can be reduced—either by weighting the loss function or by using the posterior mode as the estimate—such improvements generally come at the cost of increased overall RMSE, as discussed in App. D.

B. Estimation with predicted uncertainty

To further assess the performance and reliability of our inference frameworks, we employ estimation procedures that not only provide point estimates but also meaningful measures of predictive uncertainty. These quantifiers enable us to evaluate the *calibration* of each framework—defined by how closely the predicted uncertainty aligns with the actual spread of estimation errors (RMSE). By analysing the interplay between estimates and their associated uncertainties, we identify where specific frameworks fail to capture the underlying physics of the photoclick trajectories.

1. Approximate Bayesian Computation

In Fig. 7, we supplement the ABC RMSE curve (solid red, same as in Fig. 6) with the average variance of its reconstructed posterior (dashed red). Ideally, if the true posterior were exactly reproduced, these two curves would coincide, as the posterior variance should accurately represent the expected estimation error.

We observe that at the $n = 2$ resonance, the ABC framework heavily overestimates its uncertainty. This discrepancy indicates that the reconstructed posterior is significantly broader than the actual distribution of estimation errors. Such a mismatch suggests that while the chosen histogram statistics are sufficient to minimise the average error, they have not been sufficiently fine-tuned to fully capture the true shape and width of the posterior. This failure to reproduce the posterior width demonstrates that aggregated summary statistics discard higher-order information (here, two-photon correlations) necessary for a precise probabilistic characterisation of the system, even in regimes where the point-estimate accuracy is relatively high.

2. Probabilistic regression assuming Gaussianity

Estimating predictive uncertainty via probabilistic regression is often based on the assumption that the posterior distribution is approximately Gaussian [95]. Under this framework, the model is trained using a Negative Log-Likelihood (NLL) loss to provide both a predicted mean and variance, as described in Fig. 3(b).

In Fig. 7, we present the results for the NLL-based LSTM regressor in green. While the RMSEs, as well as the uncertainty calibration, are improved compared to the ABC method across the entire parameter range, the Gaussian assumption introduces inherent limitations. At $n = 2$, the predicted error (dashed green) is closer to the true RMSE than the ABC estimate, yet it remains significantly overestimated, indicating that the Gaussian constraint is still too rigid to perfectly match the posterior width. More notably, in the $n = 3$ regime, while the results appear relatively well-calibrated, the attained RMSE (solid green) is significantly higher than that of the MSE-trained LSTM regressor shown in Fig. 6 in blue. This demonstrates that forcing the model to produce a Gaussian-calibrated uncertainty estimate at $n = 3$ comes at the cost of point-estimate accuracy, as the Gaussian form fails to capture non-Gaussian statistics associated with three-photon correlations.

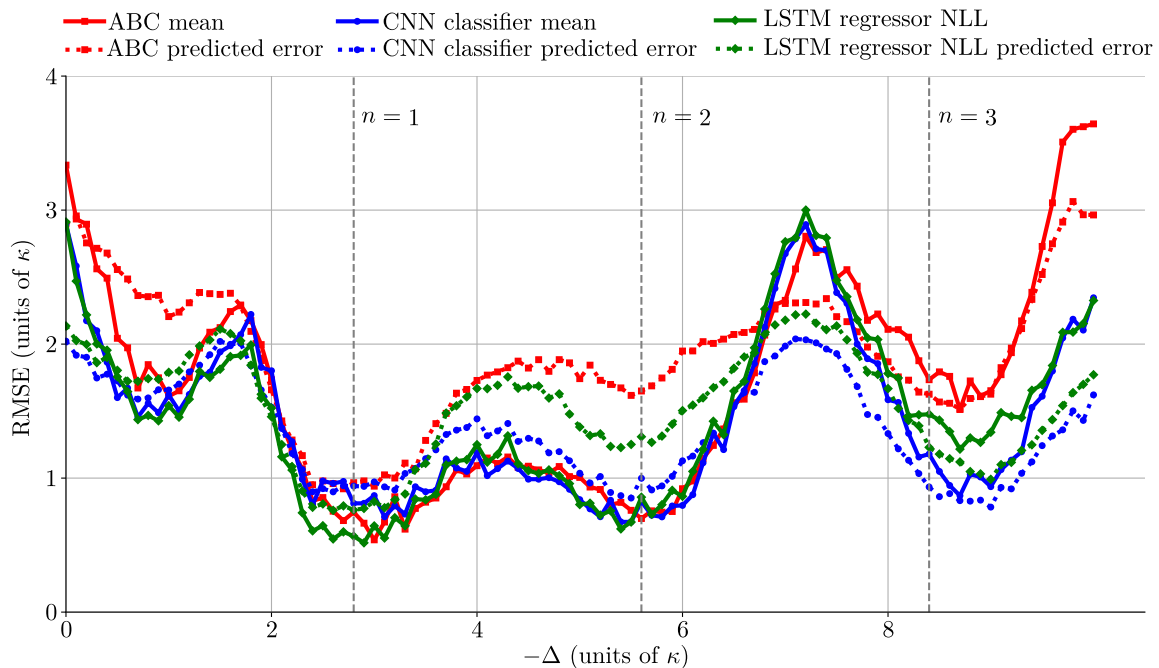


FIG. 7. **Root Mean Squared Errors (RMSEs) attained with ABC, DL-based probabilistic regression, and classification frameworks, presented alongside their predicted uncertainties** as a function of the true detuning Δ . Vertical dashed grey lines indicate the special detuning regimes ($n = 1, 2, 3$). *Solid lines* represent the RMSE for: ABC (red, same curve as in Fig. 6), the LSTM regressor trained with NLL loss (green), and the CNN classifier (blue). *Dashed lines* indicate the predicted uncertainty for each method. The CNN classifier consistently provides the lowest RMSE while maintaining high calibration across the entire parameter range; in particular, at $n = 2$ —where all three methods achieve comparable RMSE—the ABC framework (red) heavily overestimates its RMSE. Similarly, the LSTM regressor based on NLL also fails to accurately predict its error in this regime, albeit less severely, whereas the CNN continues to provide a reasonable self-estimate of its error. Overall, the LSTM regressor (solid green) outperforms the ABC framework in terms of both RMSE and uncertainty calibration across the entire parameter range. However, it is surpassed by the CNN classifier at $n = 3$, where the Gaussian approximation of the posterior fails to capture the non-Gaussian statistics associated with photons being emitted in triplets.

3. Posterior reconstruction by classification

By utilising the classification framework, we perform non-parametric posterior reconstruction by treating the network’s binned output as a probability distribution over the estimated parameter, as introduced in Fig. 3(c). The results, shown in blue in Fig. 7, demonstrate that this approach indeed avoids the accuracy-calibration trade-off encountered in probabilistic regression at the cost of high-dimensional network output.

Notably, the CNN classifier provides point estimates that achieve almost the same RMSE as the MSE-based LSTM regressor (blue curve in Fig. 6) across the entire range of the estimated detuning Δ . Unlike the previous methods, the predicted error (dashed blue) for the classifier closely tracks the attained RMSE (solid blue) even at the $n = 2$ and $n = 3$ resonances. This high degree of calibration highlights the model’s success in capturing the non-Gaussianity of the posterior, particularly for $\Delta \in (3.5, 6.5)$. By bypassing the restrictive Gaussian assumption, the classification framework successfully exploits the three-photon statistics embedded in the pho-

to-click trajectories, delivering a more reliable measure of uncertainty than both ABC and Gaussian regression.

C. Posterior reconstruction analysis

Having estimated the posterior distribution via both ABC and the CNN classifier, we now evaluate how effectively these methods reconstruct the true posterior density. To establish a ground truth for comparison, we compute the exact posterior distributions using a brute-force simulation approach [82] for a small number of photoclick trajectories. The results are visualised in Fig. 8(a-c), where we present a representative trajectory for each of the $n = 1, 2$, and 3 regimes, respectively.

Similarly to Ref. [37], we quantify the fidelity of the posterior reconstruction using the *Bhattacharyya coefficient*:

$$\mathcal{F}[p, q|D_\ell] := \int d\Delta \sqrt{p(\Delta|D_\ell) q(\Delta|D_\ell)}, \quad (25)$$

where $p(\Delta|D_\ell)$ represents the ground-truth posterior and

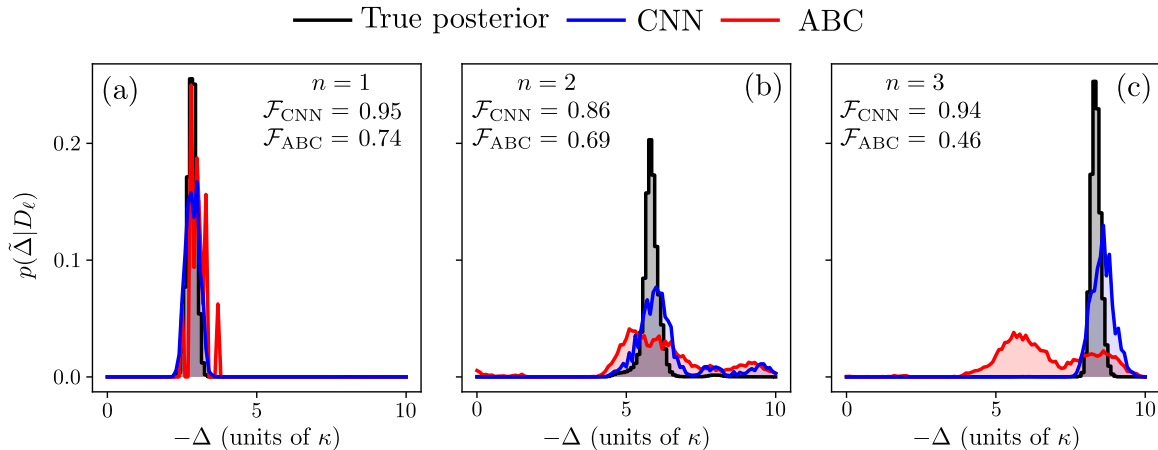


FIG. 8. **Posterior distribution reconstruction** for representative photoclick trajectories across the $n = 1, 2,$ and 3 resonance regimes. Each subplot compares the ground-truth posterior distribution (*black*) with the distributions reconstructed using ABC (*red*) and the CNN classifier (*blue*). The subplots also display the Bhattacharyya coefficient \mathcal{F} for both methods, quantifying the reconstruction fidelity. The comparison visualises the limitations of ABC at higher resonances—specifically the overestimation of variance at $n = 2$ (cf. Fig. 7) and the failure to concentrate on the true parameter value at $n = 3$ (cf. Fig. 6)—which arise because ABC relies on aggregated statistics. In contrast, the CNN closely approximates the true posterior in all regimes, including $n = 3$ at which it is able to learn the history-dependent features of the full photoclick trajectories.

$q(\Delta|D_\ell)$ is the posterior reconstructed by either ABC or the CNN classifier.

We observe that the CNN consistently outperforms ABC across all three resonance regimes ($n = 1, 2, 3$), capturing the shape of the true posterior with high accuracy and achieving superior values of \mathcal{F} . In the $n = 1$ regime, Fig. 8(a), both methods produce posteriors that are very similar to the ground truth. However, at the $n = 2$ resonance in Fig. 8(b), while the ABC framework provides a reasonably accurate point estimate, it is visually apparent from the shape of the distribution that the posterior variance is significantly overestimated. The disparity is most pronounced at $n = 3$, shown in Fig. 8(c), where ABC fails to capture both the true parameter value and the width of the distribution due to its lack of access to higher-order temporal correlations. In contrast, the CNN closely approximates then the true posterior by learning the history-dependent features within each specific photoclick pattern. All the above observations are entirely consistent with the RMSE and predicted uncertainty results presented previously in Fig. 7.

D. Robustness to dark counts

To assess the practical applicability of our inference frameworks, we evaluate their performance in the presence of *dark counts* [29, 31, 32]. These random detections follow a Poisson process at a rate λ_{DCR} dictated by thermal or electronic fluctuations. In order to consider a significant noise scenario, we follow the experimental case of Ref. [31], in which only the photons associated with the anti-Stokes sideband are detected. This leads to an increased effective dark-count rate (DCR) of 15.5 ± 0.5 Hz,

which for the $\kappa/2\pi = 2.1$ kHz applicable to that setup, yields $\lambda_{\text{DCR}} \approx 10^{-2}\kappa$. Depending on the estimated detuning Δ , this results in approximately 10 to 30 dark counts per each 80-click trajectory D_ℓ in our library.

In Fig. 9, we compare the resulting RMSE degradation for ABC (*red*), the CNN classifier (*blue*), and the LSTM regressor (*green*). Both ABC and the LSTM are remarkably resilient in the $n = 1$ and $n = 2$ regimes, with performance degradation almost exclusively confined to the $n = 3$ resonance. In contrast, the CNN exhibits a slight increase in RMSE across all regimes. This relative sensitivity is attributed to the fact that the CNN training has not yet saturated given the size of the photoclick library considered; while the LSTM has already converged, the more demanding CNN architecture would require a larger dataset to achieve similar noise resilience. We maintain a constant library size across all methods to ensure a fair comparison.

Despite the introduction of significant noise, we observe a clear dip in the RMSE at $n = 3$ for all methods, while the DL frameworks continue to outperform the ABC approach there by learning higher-order click correlations. Furthermore, we emphasise that for typical experiments employing modern photodetectors where $\lambda_{\text{DCR}} \leq 1$ Hz, the increase in estimation error due to dark counts is negligible. Indeed, our numerical tests at lower rates of $10^{-3}\kappa$ and $10^{-4}\kappa$ showed no observable change in the RMSE curves, rendering the impact of noise effectively imperceptible on the scale shown in Fig. 9.

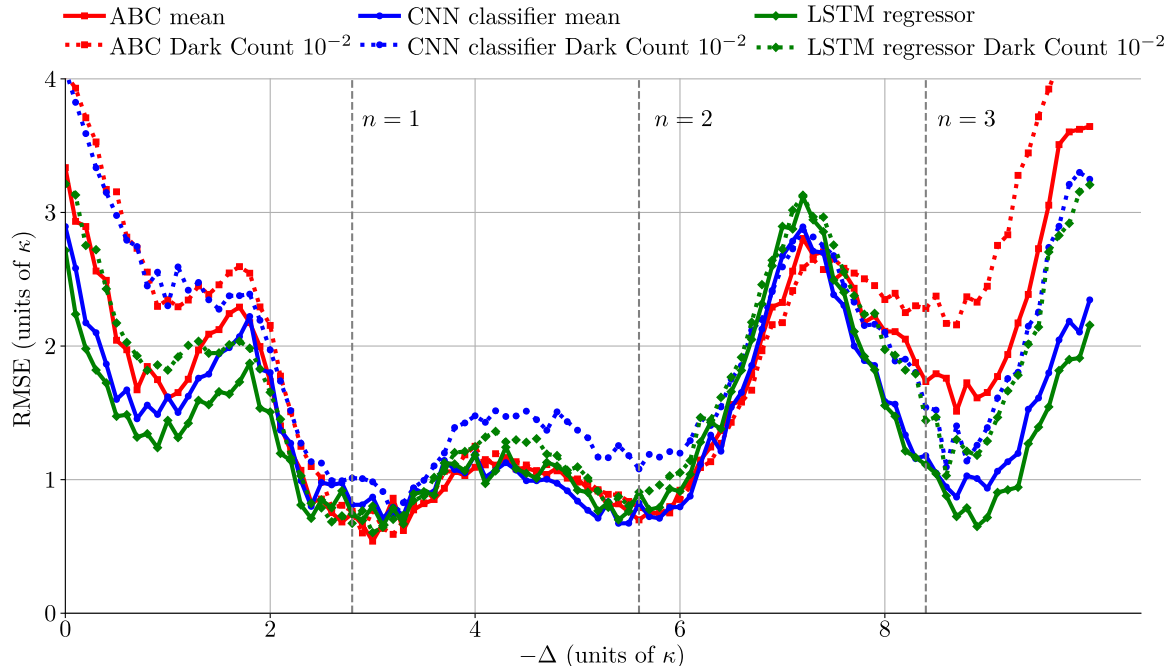


FIG. 9. **Root Mean Squared Error (RMSE) estimation with and without dark counts** at a relatively high rate (see the main text) of $\lambda_{\text{DCR}} = 10^{-2}$ (in units of κ) as a function of the parameter value Δ for ABC (red), the CNN classifier (blue), and the LSTM regressor (green). *Solid lines* represent the original noise-free datasets, while *dashed lines* indicate results including dark counts. For ABC and the LSTM, performance degradation is almost exclusively confined to the $n = 3$ regime, whereas the CNN exhibits a slight increase in RMSE across all regimes. This suggests that the CNN is currently the least robust of the three; however, this should be attributed to the fact that its training has not yet saturated for the photoclick library considered, the size of which is kept constant across all methods to ensure a fair comparison.

V. CONCLUSIONS AND OUTLOOK

In this work, we introduced a novel framework for parameter estimation in non-linear quantum sensors involving photodetection by leveraging likelihood-free inference. Specifically, we developed and compared two distinct approaches: Approximate Bayesian Computation (ABC) and various Deep Learning (DL) architectures. By systematically evaluating MSE-based regression, NLL-based regression with uncertainty estimation, and CE-based classification, we demonstrated that the optimal neural network design depends non-trivially on the specific estimation task and the statistical structure of the photoclick patterns observed.

Our results show that while both likelihood-free methods are effective, the DL models consistently outperform the ABC approach in estimation accuracy. This is particularly evident in photon-bunching regimes ($n = 2, 3$), where the networks autonomously extract and exploit relevant history-dependent quantum correlations from raw measurement data without requiring explicit prior knowledge of the system's underlying non-renewal dynamics. Once trained, the DL models achieve a 1000-fold speed-up in inference time compared to ABC (~ 25 ms versus ~ 2 s per trajectory). Furthermore, our robustness tests confirmed that both frameworks maintain high precision even under significant dark-count noise, further validat-

ing their practical applicability for realistic experimental conditions.

The primary motivation for employing such sensors, particularly in the context of optomechanics, is the high-precision estimation of external parameters and forces. Optomechanical platforms, ranging from cryogenic membranes to levitated nanospheres, have already proven to be formidable tools for sensing displacements, masses, and accelerations [101–105, 112, 113]. Our work represents a critical first step in this direction; by identifying the likelihood-free tools best suited to capturing non-classical photon statistics, we provide the necessary toolkit for real-time sensing applications.

Looking ahead, we aim to transition from fixed-length trajectory analysis to *real-time, event-by-event* estimation. This could be achieved by developing Reinforcement Learning (RL) frameworks that update parameter estimates with each detected photon, enabling truly adaptive quantum sensing [64, 114, 115]—a capability particularly valuable for tracking time-varying forces or weak gravitational fields [116]. Such an approach would allow for the estimation of coupled optomechanical dynamics where mechanical displacement encodes external force information, even in the presence of back-action effects [113].

Finally, while we have demonstrated the practical efficacy of these estimators, a rigorous comparison against

fundamental precision limits remains an open challenge. Specifically, future research should evaluate these methods against Bayesian Cramér-Rao bounds (BCRB) [117], which could potentially be derived via Gillespie-type algorithms for jump processes [39, 118]. Computing the Fisher information for photoclick trajectories is computationally demanding, as it requires monitoring both the conditional reduced state and its derivative [119, 120].

Furthermore, the question of whether photodetection constitutes the optimal measurement for a given quantum sensing task remains to be addressed. In the ideal case of pure states and fully monitored channels, this could be explored via the global Quantum Fisher Information (QFI) [120–123]. However, such computations are significantly more complex for high-dimensional systems (i.e. optomechanics), especially when accounting for unobserved degrees of freedom. Notably, this task has only recently been approached by leveraging Matrix Product Operator (MPO) representations [124] to describe the combined state of the sensor and emitted light with some unobserved degrees of freedom traced out [41, 125]. We leave the integration of these theoretical benchmarks into our framework for future investigation.

CODE AVAILABILITY

We provide the complete source code and data used for this study at [126].

ACKNOWLEDGMENTS

We would like to thank Pierre Rouchon, Patrick P. Potts, Piotr Grochowski, Marco Genoni and Klaudia Dilcher for insightful comments and suggestions. The "Novel applications of signal processing methods in quantum sensing" project is carried out within the FIRST TEAM programme of the Foundation for Polish Science co-financed by the European Union under the European Funds for Smart Economy 2021-2027 (FENG) [MM, JK]. This research is supported by the National Research Foundation, Singapore, under its Competitive Research Programme (CRP30-2023-0033) and A*STAR under its Quantum Innovation Centre (Q.InC) Strategic Research and Translational Thrust. Any opinions, findings and conclusions or recommendations expressed in this material are those of the author(s) and do not reflect the views of National Research Foundation, Singapore and A*STAR [LAC].

Appendix A: Equivalence between Cross-Entropy and KL divergence minimisation

To quantify the similarity between the ground-truth "reference" distribution $p(\varphi)$ and the network-estimated

CNN Classifier		
Layer	Output shape	Activation
Conv1D	(80, 32)	LeakyReLU
Batch Norm	-	-
MaxPool1D	(26, 32)	-
Conv1D	(26, 64)	LeakyReLU
Batch Norm	-	-
MaxPool1D	(8, 64)	-
Conv1D	(8, 64)	LeakyReLU
Batch Norm	-	-
MaxPool1D	(2, 64)	-
Flatten	128	-
Dense	200	LeakyReLU
Dense	101	SoftMax
<i>Trainable params.</i>		83,637
LSTM Regressor		
Layer	Output shape	Activation
LSTM	(80, 40)	-
LSTM	40	LeakyReLU
Batch Norm	-	-
Dense	64	LeakyReLU
Dense	16	LeakyReLU
Dense	1	-
<i>Trainable params.</i>		23,441

TABLE III. Architecture details of the LSTM regressor and CNN classifier models.

"model" distribution $q(\varphi)$, one may employ the forward ($p \rightarrow q$) *Kullback-Leibler* (KL) *divergence* defined as:

$$D_{\text{KL}}(p \parallel q) := \mathbb{E}_p \left[\log \frac{p(\varphi)}{q(\varphi)} \right] = \int d\varphi p(\varphi) \log \frac{p(\varphi)}{q(\varphi)}, \quad (\text{A1})$$

where \mathbb{E}_p denotes the expectation value with respect to the reference distribution p . Within the classification-based inference framework, p represents the target distribution over the ground-truth labels.

Specifically, given a discrete grid defining the parameter labels φ_i and an input dataset D generated with $\varphi = \varphi_{\text{true}}$, the reference is represented by an empirical distribution $p(\varphi_i|D) = \delta_{\varphi_i, \varphi_{\text{true}}}$. On the other hand, q is the network output, i.e., the model's predicted probability mass function $q(\varphi_i|D)$, which aims to approximate the true posterior distribution.

Omitting the conditioning on the input D for brevity, the empirical KL divergence then reads:

$$\begin{aligned} D_{\text{KL}}(p \parallel q) &= \sum_i [p(\varphi_i) \log p(\varphi_i) - p(\varphi_i) \log q(\varphi_i)] \\ &= -H(p) + \mathcal{L}_{\text{CE}}(p, q), \end{aligned} \quad (\text{A2})$$

where $H(p) := -\sum_i p(\varphi_i) \log p(\varphi_i)$ is the Shannon entropy of the reference distribution, and $\mathcal{L}_{\text{CE}}(p, q) = -\sum_i p(\varphi_i) \log q(\varphi_i)$ is the Cross-Entropy (CE) between reference and model distributions, defined in Eq. (17).

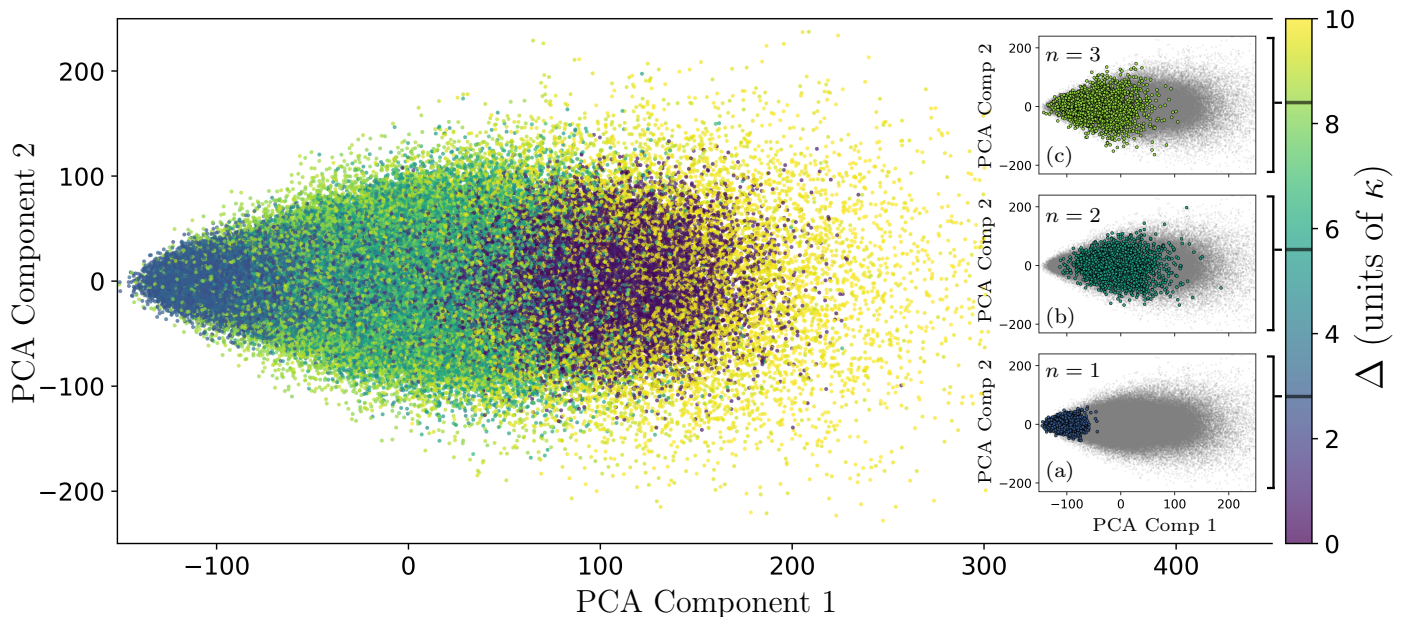


FIG. 10. **Principal Component Analysis (PCA) of the optomechanical dataset.** The main panel shows the dataset projected onto the first two principal components, with points colour-coded by the detuning parameter Δ . The first principal component (PC1) predominantly represents the total trajectory time, as the system quickly reaches a steady state where all entries contributing to PC1 become nearly identical. The spread along the PC1 axis thus reflects variations in total time for varying Δ . Insets (a), (b) and (c) display selected regions corresponding to special detuning regimes $n = 1, 2$ and 3 , respectively. Distinct clustering patterns, particularly visible for $n = 1$, highlight how total time serves as a discriminative feature across regimes. The exact detuning values yielding $n = 1, 2$ and 3 are indicated in black on the colour bar.

In our training scheme, the distribution $p(\varphi)$ is fixed by each input dataset D . Consequently, $H(p)$ is a constant with respect to the neural network parameters θ , and its gradient vanishes, $\nabla_{\theta} H(p) = 0$. Minimising the CE loss during training is therefore mathematically equivalent to minimising the KL divergence:

$$\arg \min_{\theta} \mathcal{L}_{\text{CE}}(p, q_{\theta}) = \arg \min_{\theta} D_{\text{KL}}(p \parallel q_{\theta}). \quad (\text{A3})$$

This confirms that the classification framework yields a network that approximates the true posterior distribution by minimising the information-theoretic distance between the predicted and actual probability masses.

Appendix B: Summary of neural network parameters used for the optomechanical system

In Table III, we provide the summary of NN architectures and their specs using the standard convention (see, e.g., Ref. [49]) necessary for the reconstruction of the main results concerning the optomechanical system.

Appendix C: PCA of the optomechanical dataset

To gain insight into the features leveraged by the deep learning model for parameter estimation, we perform a Principal Component Analysis (PCA) on the in-

put data (see Fig. 10). PCA identifies orthogonal directions—principal components—along which the data exhibits maximal variance, providing a compact representation of the data’s dominant structure.

In the main panel of Fig. 10, we project the dataset onto the first two principal components, with each point colour-coded by the detuning parameter Δ . The first principal component (PC1), associated with the largest eigenvalue, closely corresponds to a rescaled sum over all elements of the input vectors.

Physically, the projection onto PC1 effectively represents the *total time* of each trajectory. This behaviour arises because, after a brief transient period, the system rapidly reaches its steady state, at which point all entries contributing to PC1 become nearly identical. Consequently, the PCA primarily captures variations in the cumulative waiting times that compose each trajectory, making PC1 a natural representation of the total time.

The spread of points along the PC1 axis reflects changes in the trajectory’s total time for different detunings Δ . Meanwhile, the inset plots in Fig. 10(a–c) display data subsets corresponding to special photon regimes $n = 1, 2$ and 3 . Distinct clustering patterns emerge, particularly for $n = 1$, where trajectories are well separated from those in the $n = 2$ and $n = 3$ regimes. This observation indicates that when estimating detuning values in the $n = 1$ regime, the total time can serve as a sufficient statistics.

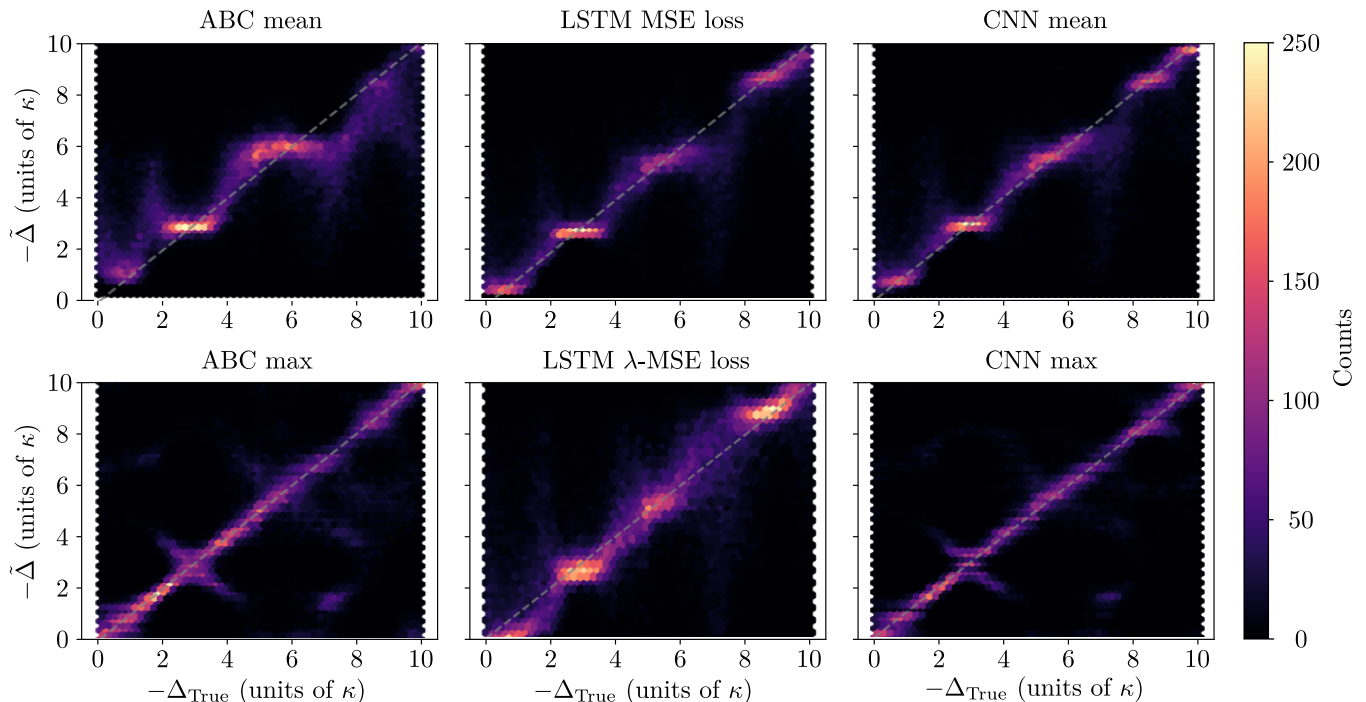


FIG. 11. **Parameter estimation across various inference frameworks.** Comparison of parameter estimation for different detunings, $\Delta_{\text{True}} \in [0, 10]$, when leveraging ABC (left), regression (middle), or classification (right) methods. Each subplot displays the joint distribution of the true parameter Δ_{True} (horizontal axis) and its estimator $\hat{\Delta}$ (vertical axis) provided by a given method. The colour intensity indicates the density of estimates, with lighter regions denoting higher frequencies; the dashed diagonal line represents ideal estimation. *Left column (ABC)*: Estimator $\hat{\Delta}$ provided by either the mean (top) or mode (bottom) of the reconstructed posterior, using total time and the waiting-time histogram as summary statistics. *Middle column (regression)*: LSTM-based regression employing a standard MSE loss (top) or a modified loss function designed to mitigate bias (bottom). *Right column (classification)*: CNN-based classification with point estimates being provided either by the mean (top) or the mode (bottom) of the predicted posterior distribution.

Appendix D: Reducing bias in estimation

As an additional analysis, we compare different inference methods in terms of their parameter estimation behaviour, visualised via 2D density plots in Fig. 11. These plots map the relationship between the true detuning value Δ and the corresponding estimated value $\hat{\Delta}$ across multiple trials, allowing for a visual assessment of the inference structure. In Bayesian parameter estimation, one typically chooses between the mean or the mode of the posterior distribution as the point estimator. While the mean is theoretically optimal under the MSE loss, the mode often yields more representative values in cases of skewed or multimodal distributions.

Using ABC to reconstruct the posterior distribution and taking its mean as the parameter estimator (Fig. 11, top-left), we observe distinct horizontal regions—plateaus—specifically around the $n = 1, 2$, and 3 regimes. These plateaus indicate a lack of sensitivity to changes in the true parameter. Interestingly, these artefacts disappear (at the cost of a slightly higher MSE) when the mode of the reconstructed posterior is used instead (Fig. 11, bottom-left). A similar behaviour is observed when reconstructing the posterior with a CNN

(Fig. 11, bottom-right). Nonetheless, because the CNN is capable of learning higher-order correlations between photoclicks, its performance significantly exceeds that of ABC in the $n = 3$ regime, when interpreting the posterior mean as the estimator $\hat{\Delta}$ (Fig. 11, top-right).

Regarding the LSTM regressor trained with a standard MSE loss (Fig. 11, top-middle), the appearance of plateaus suggests that the network is effectively learning to approximate the posterior mean. To understand and mitigate this effect, we consider the decomposition of the MSE [127]:

$$\text{MSE}(\hat{\Delta}) = \text{Var}(\hat{\Delta}) + [\text{Bias}(\hat{\Delta}, \Delta)]^2, \quad (\text{D1})$$

where Δ is the true parameter and $\hat{\Delta}$ is its estimate.

The emergence of plateaus in all top plots Fig. 11 indicates that these architectures prioritise low variance at the expense of high bias in certain parameter regions. To address this issue in regression, we introduce a modified loss function that explicitly balances bias and variance via a weighting factor λ , i.e.:

$$\text{MSE}_\lambda(\hat{\Delta}) = \lambda \text{Var}(\hat{\Delta}) + [\text{Bias}(\hat{\Delta}, \Delta)]^2. \quad (\text{D2})$$

With $\lambda = 0.8$ (favouring bias reduction), the LSTM regressor yields a smoother estimator (Fig. 11, bottom-middle), significantly reducing plateau artefacts and mirroring the behaviour when it is rather the mode of posterior used as the estimator $\hat{\Delta}$.

Despite the improved qualitative behaviour, this modification does not lead to a significant reduction in the

Root Mean Squared Error (RMSE). Nonetheless, this analysis provides insight into how does the objective function design dictates the structure of learned estimators and demonstrates how different posterior summary statistics (mean vs. mode) manifest in learning-based inference.

-
- [1] V. Giovannetti, S. Lloyd, and L. Maccone, “Quantum-Enhanced Positioning and Clock Synchronization,” *Nature* **412**, 417 (2001).
- [2] V. Giovannetti, S. Lloyd, and L. Maccone, “Quantum Metrology,” *Phys. Rev. Lett.* **96**, 010401 (2006).
- [3] J. P. Dowling, “Quantum Optical Metrology—The Lowdown on High-*N00N* States,” *Contemp. Phys.* **49**, 125 (2008).
- [4] V. Giovannetti, S. Lloyd, and L. Maccone, “Advances in Quantum Metrology,” *Nat. Photonics* **5**, 222 (2011).
- [5] L. Pezzè, A. Smerzi, M. K. Oberthaler, R. Schmied, and P. Treutlein, “Quantum Metrology with Nonclassical States of Atomic Ensembles,” *Rev. Mod. Phys.* **90**, 035005 (2018).
- [6] I. D. Leroux, M. H. Schleier-Smith, and V. Vuletić, “Implementation of Cavity Squeezing of a Collective Atomic Spin,” *Phys. Rev. Lett.* **104**, 073602 (2010).
- [7] O. Hosten, N. J. Engelsen, R. Krishnakumar, and M. A. Kasevich, “Measurement Noise 100 Times Lower Than the Quantum-Projection Limit Using Entangled Atoms,” *Nature* **529**, 505 (2016).
- [8] E. Pedrozo-Peñafiel, et al., “Entanglement on an Optical Atomic-Clock Transition,” *Nature* **588**, 414 (2020).
- [9] S. Colombo, E. Pedrozo-Peñafiel, and V. Vuletić, “Entanglement-Enhanced Optical Atomic Clocks,” *Appl. Phys. Lett.* **121**, 210502 (2022).
- [10] R. Sewell, M. Koschorreck, M. Napolitano, B. Dubost, N. Behhood, and M. Mitchell, “Magnetic Sensitivity beyond the Projection Noise Limit by Spin Squeezing,” *Phys. Rev. Lett.* **109**, 253605 (2012).
- [11] F. Martin Ciurana, G. Colangelo, L. Slodička, R. J. Sewell, and M. W. Mitchell, “Entanglement-Enhanced Radio-Frequency Field Detection and Waveform Sensing,” *Phys. Rev. Lett.* **119**, 043603 (2017).
- [12] W. Wu, et al., “Spin Squeezing in an Ensemble of Nitrogen-Vacancy Centres in Diamond,” *Nature* **646**, 74 (2025).
- [13] H. Gao, et al., “Signal Amplification in a Solid-State Sensor through Asymmetric Many-Body Echo,” *Nature* **646**, 68 (2025).
- [14] C. Gross, T. Zibold, E. Nicklas, J. Estève, and M. K. Oberthaler, “Nonlinear Atom Interferometer Surpasses Classical Precision Limit,” *Nature* **464**, 1165 (2010).
- [15] R. Demkowicz-Dobrzański, M. Jarzyna, and J. Kołodyński, “Quantum Limits in Optical Interferometry,” in *Progress in Optics*, Vol. 60, edited by E. Wolf (Elsevier, 2015) pp. 345–435, [arXiv:1405.7703 \[quant-ph\]](https://arxiv.org/abs/1405.7703).
- [16] K. Bongs, M. Holynski, J. Vovrosh, P. Bouyer, G. Condon, E. Rasel, C. Schubert, W. P. Schleich, and A. Roura, “Taking Atom Interferometric Quantum Sensors from the Laboratory to Real-World Applications,” *Nat. Rev. Phys.* **3**, 814 (2021).
- [17] M. Tse, et al., “Quantum-Enhanced Advanced LIGO Detectors in the Era of Gravitational-Wave Astronomy,” *Phys. Rev. Lett.* **123**, 231107 (2019).
- [18] D. Ganapathy, et al. (LIGO O4 Detector Collaboration), “Broadband Quantum Enhancement of the LIGO Detectors with Frequency-Dependent Squeezing,” *Phys. Rev. X* **13**, 041021 (2023).
- [19] W. Wiecek, S. G. Hofer, J. Hoelscher-Obermaier, R. Riedinger, K. Hammerer, and M. Aspelmeyer, “Optimal State Estimation for Cavity Optomechanical Systems,” *Phys. Rev. Lett.* **114**, 223601 (2015).
- [20] M. Rossi, D. Mason, J. Chen, and A. Schliesser, “Observing and Verifying the Quantum Trajectory of a Mechanical Resonator,” *Phys. Rev. Lett.* **123**, 163601 (2019).
- [21] L. Magrini, P. Rosenzweig, C. Bach, A. Deutschmann-Olek, S. G. Hofer, S. Hong, N. Kiesel, A. Kugi, and M. Aspelmeyer, “Real-Time Optimal Quantum Control of Mechanical Motion at Room Temperature,” *Nature* **595**, 373 (2021).
- [22] F. Tebbenjohanns, M. L. Mattana, M. Rossi, M. Frimmer, and L. Novotny, “Quantum Control of a Nanoparticle Optically Levitated in Cryogenic Free Space,” *Nature* **595**, 378 (2021).
- [23] V. B. Braginsky and F. Y. Khalili, *Quantum Measurement*, edited by K. Thorne (Cambridge University Press, 1995).
- [24] H. M. Wiseman and G. J. Milburn, *Quantum Measurement and Control* (Cambridge University Press, 2009).
- [25] A. Ferraro, S. Olivares, and M. G. A. Paris, *Gaussian States in Continuous Variable Quantum Information* (Bibliopolis, Napoli, 2005) <http://arxiv.org/abs/quant-ph/0503237>.
- [26] C. Weedbrook, S. Pirandola, R. García-Patrón, N. J. Cerf, T. C. Ralph, J. H. Shapiro, and S. Lloyd, “Gaussian Quantum Information,” *Rev. Mod. Phys.* **84**, 621 (2012).
- [27] R. H. Hadfield, “Single-Photon Detectors for Optical Quantum Information Applications,” *Nat. Photonics* **3**, 696 (2009).
- [28] in *Advanced Time-Correlated Single Photon Counting Techniques*, edited by W. Becker, A. W. Castleman, J. Toennies, and W. Zinth (Springer, Berlin, Heidelberg, 2005) pp. 61–212.
- [29] J. D. Cohen, S. M. Meenehan, G. S. MacCabe, S. Gröblacher, A. H. Safavi-Naeini, F. Marsili, M. D. Shaw, and O. Painter, “Phonon Counting and Intensity Interferometry of a Nanomechanical Resonator,” *Nature* **520**, 522 (2015).
- [30] R. Riedinger, A. Wallucks, I. Marinković, C. Löschnauer, M. Aspelmeyer, S. Hong, and

- S. Gröblacher, “Remote Quantum Entanglement between Two Micromechanical Oscillators,” *Nature* **556**, 473 (2018).
- [31] I. Galinskiy, Y. Tsaturyan, M. Parniak, and E. S. Polzik, “Phonon Counting Thermometry of an Ultracoherent Membrane Resonator near Its Motional Ground State,” *Optica* **7**, 718 (2020).
- [32] N. Fiaschi, B. Hensen, A. Wallucks, R. Benevides, J. Li, T. P. M. Alegre, and S. Gröblacher, “Optomechanical Quantum Teleportation,” *Nat. Photonics* **15**, 817 (2021).
- [33] G. Ortolano, E. Losero, S. Pirandola, M. Genovese, and I. Ruo-Berchera, “Experimental Quantum Reading with Photon Counting,” *Sci. Adv.* **7**, eabc7796 (2021).
- [34] I. Galinskiy, G. Enzian, M. Parniak, and E. S. Polzik, “Nonclassical Correlations between Photons and Phonons of Center-Of-Mass Motion of a Mechanical Oscillator,” *Phys. Rev. Lett.* **133**, 173605 (2024).
- [35] A. H. Kiilerich and K. Mølmer, “Estimation of Atomic Interaction Parameters by Photon Counting,” *Phys. Rev. A* **89**, 052110 (2014).
- [36] M. B. Plenio and P. L. Knight, “The Quantum-Jump Approach to Dissipative Dynamics in Quantum Optics,” *Rev. Mod. Phys.* **70**, 101 (1998).
- [37] L. A. Clark and J. Kołodyński, “Efficient Inference of Quantum System Parameters by Approximate Bayesian Computation,” *Phys. Rev. Applied* **23**, 044040 (2025).
- [38] E. Rinaldi, M. González Lastre, S. García Herberos, S. Ahmed, M. Khanahmadi, F. Nori, and C. Sánchez Muñoz, “Parameter Estimation from Quantum-Jump Data Using Neural Networks,” *Quantum Sci. Technol.* **9**, 035018 (2024).
- [39] M. Radaelli, J. A. Smiga, G. T. Landi, and F. C. Binder, “Parameter Estimation for Quantum Jump Unraveling,” [10.48550/arxiv.2402.06556](https://arxiv.org/abs/2402.06556) (2024), [arXiv:2402.06556](https://arxiv.org/abs/2402.06556) [quant-ph].
- [40] A. Anteneh, “Parameter Estimation with Uncertainty Quantification from Continuous Measurement Data Using Neural Network Ensembles,” [10.48550/arxiv.2509.10756](https://arxiv.org/abs/2509.10756) (2025), [arXiv:2509.10756](https://arxiv.org/abs/2509.10756) [quant-ph].
- [41] A. Khan, F. Albarelli, and A. Datta, “Tensor Network Approach to Sensing Quantum Light-Matter Interactions,” *PRX Quantum* **6**, 040343 (2025).
- [42] V. Gebhart, R. Santagati, A. A. Gentile, E. M. Gauger, D. Craig, N. Ares, L. Banchi, F. Marquardt, L. Pezzè, and C. Bonato, “Learning Quantum Systems,” *Nat. Rev. Phys.* **5**, 141 (2023).
- [43] W. R. Gilks, S. Richardson, and D. J. Spiegelhalter, *Markov Chain Monte Carlo in Practice* (CRC Press, 1995).
- [44] K. P. Murphy, *Machine Learning: A Probabilistic Perspective* (The MIT Press, 2012).
- [45] C. Granade, C. Ferrie, I. Hincks, S. Casagrande, T. Alexander, J. Gross, M. Kononenko, and Y. Sanders, “Qinfer: Statistical Inference Software for Quantum Applications,” *Quantum* **1**, 5 (2017).
- [46] S. A. Sisson, Y. Fan, and M. Beaumont, *Handbook of Approximate Bayesian Computation* (CRC Press, 2018).
- [47] B. M. Turner and T. Van Zandt, “A Tutorial on Approximate Bayesian Computation,” *J. Math. Psychol.* **56**, 69 (2012).
- [48] M. A. Beaumont, W. Zhang, and D. J. Balding, “Approximate Bayesian Computation in Population Genetics,” *Genetics* **162**, 2025 (2002).
- [49] I. Goodfellow, Y. Bengio, and A. Courville, *Deep Learning* (MIT Press, 2016).
- [50] C. E. Granade, C. Ferrie, N. Wiebe, and D. G. Cory, “Robust Online Hamiltonian Learning,” *New J. Phys.* **14**, 103013 (2012).
- [51] A. Sergeevich, A. Chandran, J. Combes, S. D. Bartlett, and H. M. Wiseman, “Characterization of a Qubit Hamiltonian Using Adaptive Measurements in a Fixed Basis,” *Phys. Rev. A* **84**, 052315 (2011).
- [52] N. Wiebe and C. Granade, “Efficient Bayesian Phase Estimation,” *Phys. Rev. Lett.* **117**, 010503 (2016).
- [53] M. Khanahmadi and K. Mølmer, “Time-Dependent Atomic Magnetometry with a Recurrent Neural Network,” *Phys. Rev. A* **103**, 032406 (2021).
- [54] S. Nolan, A. Smerzi, and L. Pezzè, “A Machine Learning Approach to Bayesian Parameter Estimation,” *npj Quantum Inf.* **7**, [10.1038/s41534-021-00497-w](https://doi.org/10.1038/s41534-021-00497-w) (2021).
- [55] C. Huerta Alderete, M. H. Gordon, F. Sauvage, A. Sone, A. T. Sornborger, P. J. Coles, and M. Cerezo, “Inference-Based Quantum Sensing,” *Phys. Rev. Lett.* **129**, 190501 (2022).
- [56] I. Khalid, C. A. Weidner, E. A. Jonckheere, S. G. Schirmer, and F. C. Langbein, “Sample-Efficient Model-Based Reinforcement Learning for Quantum Control,” *Phys. Rev. Research* **5**, 043002 (2023).
- [57] I. Nikoloska, H. Joudeh, R. van Sloun, and O. Simeone, “Dynamic Estimation Loss Control in Variational Quantum Sensing Via Online Conformal Inference,” [10.48550/arXiv.2505.23389](https://arxiv.org/abs/2505.23389) (2025), [arXiv:2505.23389](https://arxiv.org/abs/2505.23389) [quant-ph].
- [58] Z. Zhou, Y. Du, X.-F. Yin, S. Zhao, X. Tian, and D. Tao, “Optical Quantum Sensing for Agnostic Environments Via Deep Learning,” *Phys. Rev. Research* **6**, 043267 (2024).
- [59] H. Xu, L. Wang, H. Yuan, and X. Wang, “Generalizable Control for Multiparameter Quantum Metrology,” *Phys. Rev. A* **103**, 042615 (2021).
- [60] T. Xiao, J. Fan, and G. Zeng, “Parameter Estimation in Quantum Sensing Based on Deep Reinforcement Learning,” *npj Quantum Inf.* **8**, 2 (2022).
- [61] L. J. Fiderer, J. Schuff, and D. Braun, “Neural-Network Heuristics for Adaptive Bayesian Quantum Estimation,” *PRX Quantum* **2**, 020303 (2021).
- [62] A. Lumino, E. Polino, A. S. Rab, G. Milani, N. Spagnolo, N. Wiebe, and F. Sciarrino, “Experimental Phase Estimation Enhanced by Machine Learning,” *Phys. Rev. Applied* **10**, 044033 (2018).
- [63] V. Cimini, I. Gianani, N. Spagnolo, F. Leccese, F. Sciarrino, and M. Barbieri, “Calibration of Quantum Sensors by Neural Networks,” *Phys. Rev. Lett.* **123**, 230502 (2019).
- [64] V. Cimini, M. Valeri, E. Polino, S. Piacentini, F. Ceccarelli, G. Corrielli, N. Spagnolo, R. Osellame, and F. Sciarrino, “Deep Reinforcement Learning for Quantum Multiparameter Estimation,” *Adv. Photonics* **5**, 016005 (2023).
- [65] D. E. Chang, V. Vuletić, and M. D. Lukin, “Quantum Nonlinear Optics — Photon by Photon,” *Nat. Photonics* **8**, 685 (2014).
- [66] M. Aspelmeyer, T. J. Kippenberg, and F. Marquardt, “Cavity Optomechanics,” *Rev. Mod. Phys.* **86**, 1391 (2014).

- [67] H. Paul, “Photon antibunching,” *Rev. Mod. Phys.* **54**, 1061 (1982).
- [68] C. T. Lee, “External photodetection of cavity radiation,” *Phys. Rev. A* **48**, 2285 (1993).
- [69] D. Chruściński and S. Pascazio, “A Brief History of the GKLS Equation,” *Open Syst. Inf. Dyn.* **24**, 1740001 (2017).
- [70] Alternatively, one may consider Eq. (3) as a starting point to describe system dynamics.
- [71] H. J. Carmichael, *Statistical Methods in Quantum Optics 2* (Springer Berlin Heidelberg, 2008).
- [72] C. W. Gardiner, *Handbook of Stochastic Methods for Physics, Chemistry and the Natural Sciences* (Springer Berlin Heidelberg, 1985).
- [73] J. Dalibard, Y. Castin, and K. Mølmer, “Wave-Function Approach to Dissipative Processes in Quantum Optics,” *Phys. Rev. Lett.* **68**, 580 (1992).
- [74] K. Mølmer, Y. Castin, and J. Dalibard, “Monte Carlo Wave-Function Method in Quantum Optics,” *J. Opt. Soc. Am. B* **10**, 524 (1993).
- [75] G. C. Hegerfeldt, “How to Reset an Atom After a Photon Detection: Applications to Photon-Counting Processes,” *Phys. Rev. A* **47**, 449 (1993).
- [76] D. J. Daley and D. Vere-Jones, *An Introduction to the Theory of Point Processes* (Springer, New York NY, 2005).
- [77] H. J. Carmichael, S. Singh, R. Vyas, and P. R. Rice, “Photoelectron waiting times and atomic state reduction in resonance fluorescence,” *Phys. Rev. A* **39**, 1200 (1989).
- [78] G. T. Landi, M. J. Kewming, M. T. Mitchison, and P. P. Potts, “Current Fluctuations in Open Quantum Systems: Bridging the Gap between Quantum Continuous Measurements and Full Counting Statistics,” *PRX Quantum* **5**, 020201 (2024).
- [79] D. Burgarth, V. Giovannetti, A. N. Kato, and K. Yuasa, “Quantum estimation via sequential measurements,” *New J. Phys.* **17**, 113055 (2015).
- [80] A. H. Kiilerich and K. Mølmer, “Bayesian parameter estimation by continuous homodyne detection,” *Phys. Rev. A* **94**, 032103 (2016).
- [81] L. A. Clark, A. Stokes, and A. Beige, “Quantum jump metrology,” *Phys. Rev. A* **99**, 022102 (2019).
- [82] L. A. Clark, B. Markowicz, and J. Kołodyński, “Exploiting Non-Linear Effects in Optomechanical Sensors with Continuous Photon-Counting,” *Quantum* **6**, 812 (2022).
- [83] L. Mandel and E. Wolf, *Optical Coherence and Quantum Optics* (Cambridge University Press, Cambridge, 1995).
- [84] M. C. Teich, B. E. A. Saleh, and J. Peřina, “Role of Primary Excitation Statistics in the Generation of Antibunched and Sub-Poisson Light,” *J. Opt. Soc. Am. B* **1**, 366 (1984).
- [85] J. Cao, “Correlations in Single Molecule Photon Statistics: Renewal Indicator,” *J. Phys. Chem. B* **110**, 19040 (2006).
- [86] S. M. Kay, *Fundamentals of Statistical Signal Processing* (Prentice-Hall, Inc., 1993).
- [87] A. Dawid, et al., *Machine Learning in Quantum Sciences* (Cambridge University Press, Cambridge, 2025).
- [88] A. M. Palmieri, G. Müller-Rigat, A. K. Srivastava, M. Lewenstein, G. Rajchel-Mieldzioć, and M. Płodzień, “Enhancing Quantum State Tomography Via Resource-Efficient Attention-Based Neural Networks,” *Phys. Rev. Research* **6**, 033248 (2024).
- [89] P. Huembeli, A. Dauphin, and P. Wittek, “Identifying quantum phase transitions with adversarial neural networks,” *Phys. Rev. B* **97**, 134109 (2018).
- [90] K. Kottmann, P. Huembeli, M. Lewenstein, and A. Acín, “Unsupervised Phase Discovery with Deep Anomaly Detection,” *Phys. Rev. Lett.* **125**, 170603 (2020).
- [91] A. Fallani, M. A. C. Rossi, D. Tamascelli, and M. G. Genoni, “Learning Feedback Control Strategies for Quantum Metrology,” *PRX Quantum* **3**, 020310 (2022).
- [92] P. Vaidhyathan, F. Marquardt, M. T. Mitchison, and N. Ares, “Quantum Feedback Control with a Transformer Neural Network Architecture,” 10.48550/arxiv.2411.19253 (2024), arXiv:2411.19253 [quant-ph].
- [93] J. Duan, Z. Hu, X. Lu, L. Xiao, S. Jia, K. Mølmer, and Y. Xiao, “Concurrent Spin Squeezing and Field Tracking with Machine Learning,” *Nat. Phys.* **21**, 909 (2025).
- [94] C. Mingard, G. Valle-Pérez, J. Skalse, and A. A. Louis, “Is Sgd a Bayesian Sampler? Well, Almost,” *J. Mach. Learn. Res.* **22**, 1 (2021), arXiv:2006.15191 [cs.LG].
- [95] C. Kneissl, C. Bülte, P. Scholl, and G. Kutyniok, “Improved probabilistic regression using diffusion models,” in *Northern Lights Deep Learning Conference Abstracts 2026* (2025).
- [96] D. Nix and A. Weigend, “Estimating the mean and variance of the target probability distribution,” in *Proceedings of 1994 IEEE International Conference on Neural Networks (ICNN’94)*, Vol. 1 (1994) pp. 55–60 vol.1.
- [97] B. Lakshminarayanan, A. Pritzel, and C. Blundell, “Simple and Scalable Predictive Uncertainty Estimation using Deep Ensembles,” in *Advances in Neural Information Processing Systems*, Vol. 30, edited by I. Guyon, U. V. Luxburg, S. Bengio, H. Wallach, R. Fergus, S. Vishwanathan, and R. Garnett (Curran Associates, Inc., 2017).
- [98] S. Hochreiter and J. Schmidhuber, “Long Short-Term Memory,” *Neural Comput.* **9**, 1735 (1997).
- [99] H.-P. Breuer and F. Petruccione, *The Theory of Open Quantum Systems* (Oxford University Press Oxford, 2007).
- [100] A. Kronwald, M. Ludwig, and F. Marquardt, “Full Photon Statistics of a Light Beam Transmitted through an Optomechanical System,” *Phys. Rev. A* **87**, 013847 (2013).
- [101] B. Guha, P. E. Allain, A. Lemaître, G. Leo, and I. Favero, “Force Sensing with an Optomechanical Self-Oscillator,” *Phys. Rev. Applied* **14**, 024079 (2020).
- [102] D. Hälg, et al., “Membrane-Based Scanning Force Microscopy,” *Phys. Rev. Applied* **15**, 1021001 (2021).
- [103] N. Kampel, R. Peterson, R. Fischer, P.-L. Yu, K. Cicak, R. Simmonds, K. Lehnert, and C. Regal, “Improving Broadband Displacement Detection with Quantum Correlations,” *Phys. Rev. X* **7**, 021008 (2017).
- [104] D. Mason, J. Chen, M. Rossi, Y. Tsaturyan, and A. Schliesser, “Continuous Force and Displacement Measurement below the Standard Quantum Limit,” *Nat. Phys.* **15**, 745 (2019).
- [105] Y. Xia, A. R. Agrawal, C. M. Pluchar, A. J. Brady, Z. Liu, Q. Zhuang, D. J. Wilson, and Z. Zhang, “Entanglement-Enhanced Optomechanical Sensing,” *Nat. Photonics* **17**, 470 (2023).
- [106] A. J. Brady, et al., “Entanglement-Enhanced Optomechanical Sensor Array with Application to Dark Mat-

- ter Searches,” *Commun. Phys.* **6**, 10.1038/s42005-023-01357-z (2023).
- [107] E. Hebestreit, M. Frimmer, R. Reimann, and L. Novotny, “Sensing Static Forces with Free-Falling Nanoparticles,” *Phys. Rev. Lett.* **121**, 063602 (2018).
- [108] Y.-H. Tseng, T. Penny, B. Siegel, J. Wang, and D. C. Moore, “Search for Dark Matter Scattering from Optically Levitated Nanoparticles,” *PRX Quantum* **6**, 040367 (2025).
- [109] A. G. Krause, T. D. Blasius, and O. Painter, “A high-bandwidth sub-femtometre displacement sensor is based on a photonic crystal cavity,” *Nat. Photonics* **6**, 768 (2012).
- [110] J. Guo, R. A. Norte, and S. Gröblacher, “Integrated optical force sensors using focusing photonic crystal arrays,” *Opt. Express* **25**, 9196 (2017).
- [111] S. Hong, R. Riedinger, I. Marinković, A. Wallucks, S. G. Hofer, R. A. Norte, M. Aspelmeyer, and S. Gröblacher, “Hanbury Brown and Twiss interferometry of single phonons from an optomechanical resonator,” *Science* **358**, 203 (2017).
- [112] S. Barzanjeh, A. Xuereb, S. Gröblacher, M. Paternostro, C. A. Regal, and E. M. Weig, “Optomechanics for Quantum Technologies,” *Nat. Phys.* **18**, 15 (2021).
- [113] J. Cripe, N. Aggarwal, R. Lanza, A. Libson, R. Singh, P. Heu, D. Follman, G. D. Cole, N. Mavalvala, and T. Corbitt, “Measurement of Quantum Back Action in the Audio Band at Room Temperature,” *Nature* **568**, 364 (2019).
- [114] F. Belliardo, F. Zoratti, and V. Giovannetti, “Applications of Model-Aware Reinforcement Learning in Bayesian Quantum Metrology,” *Phys. Rev. A* **109**, 062609 (2024).
- [115] F. Belliardo, F. Zoratti, F. Marquardt, and V. Giovannetti, “Model-Aware Reinforcement Learning for High-Performance Bayesian Experimental Design in Quantum Metrology,” *Quantum* **8**, 1555 (2024).
- [116] S. Qvarfort, A. Serafini, P. F. Barker, and S. Bose, “Gravimetry through Non-Linear Optomechanics,” *Nat. Commun.* **9**, 3690 (2018).
- [117] H. L. van Trees, *Detection, Estimation and Modulation Theory*, Vol. I (Wiley, 1968).
- [118] M. Radaelli, G. T. Landi, and F. C. Binder, “Gillespie Algorithm for Quantum Jump Trajectories,” *Phys. Rev. A* **110**, 062212 (2024).
- [119] S. Gammelmark and K. Mølmer, “Bayesian Parameter Inference from Continuously Monitored Quantum Systems,” *Phys. Rev. A* **87**, 032115 (2013).
- [120] F. Albarelli, M. A. C. Rossi, D. Tamascelli, and M. G. Genoni, “Restoring Heisenberg Scaling in Noisy Quantum Metrology by Monitoring the Environment,” *Quantum* **2**, 110 (2018).
- [121] S. Gammelmark and K. Mølmer, “Fisher Information and the Quantum Cramér-Rao Sensitivity Limit of Continuous Measurements,” *Phys. Rev. Lett.* **112**, 170401 (2014).
- [122] T. Ilias, D. Yang, S. F. Huelga, and M. B. Plenio, “Criticality-Enhanced Quantum Sensing Via Continuous Measurement,” *PRX Quantum* **3**, 010354 (2022).
- [123] D. Yang, S. F. Huelga, and M. B. Plenio, “Efficient Information Retrieval for Sensing Via Continuous Measurement,” *Phys. Rev. X* **13**, 031012 (2023).
- [124] J. I. Cirac, D. Pérez-García, N. Schuch, and F. Verstraete, “Matrix product states and projected entangled pair states: Concepts, symmetries, theorems,” *Rev. Mod. Phys.* **93**, 045003 (2021).
- [125] D. Yang, M. Ketkar, K. Audenaert, S. F. Huelga, and M. B. Plenio, “Quantum Cramer-Rao Precision Limit of Noisy Continuous Sensing,” 10.48550/arXiv.2504.12400 (2025), arXiv:2504.12400 [quant-ph].
- [126] <https://github.com/QI2-lab/Nonlinear-optomechanical-parameter-estimation>.
- [127] D. D. Wackerly, W. Mendenhall, and R. L. Scheafner, *Mathematical Statistics with Applications* (Thomson Brooks/Cole, 2001).